

# Enrichment strategies and convergence properties of the XFEM for hydraulic fracture problems

Elizaveta Gordeliy and Anthony Peirce\*

*Department of Mathematics, University of British Columbia, Vancouver, British Columbia, Canada V6T 1Z2*

---

## Abstract

In two recent papers [1, 2] investigating the use of Extended Finite Element Method (XFEM) for modeling hydraulic fractures (HF), two classes of boundary value problem and two distinct enrichment types were identified as being essential components in constructing successful XFEM HF algorithms. In this paper we explore the accuracy and convergence properties of these boundary value formulations and enrichment strategies. In addition, we derive a novel set of crack-tip enrichment functions that enable the XFEM to model HF with the full range of power law  $r^\lambda$  behavior of the displacement field and the corresponding  $r^{\lambda-1}$  singularity in the stress field, for  $\frac{1}{2} \leq \lambda < 1$ . This novel crack-tip enrichment enables the XFEM to achieve the optimal convergence rate, which is not achieved by existing enrichment functions used for this range of power law. The two XFEM boundary value problem classes are as follows: i) a Neumann to Dirichlet map in which the pressure applied to the crack faces is the specified boundary condition and the XFEM is used to solve for the corresponding crack width ( $P \rightarrow W$ ); and ii) a mixed hybrid formulation of the XFEM that makes it possible to incorporate the singular behavior of the crack width in the fracture tip and uses a pressure boundary condition away from it ( $P\&W$ ). The two enrichment schemes considered are: i) the *XFEM-t* scheme with full singular crack-tip enrichment and ii) a simpler, more efficient, *XFEM-s* scheme in which the singular tip behavior is only imposed in a weak sense. If enrichment is applied to all the nodes of tip-enriched elements, then the resulting XFEM stiffness matrix is singular due to a linear dependence among the set of enrichment shape functions, which

---

\*Corresponding Author. E-mail:peirce@math.ubc.ca Tel.:+1 604 822 2104

is a situation that also holds for the classic set of square-root enrichment functions. For the novel set of enrichment functions we show how to remove this rank deficiency by eliminating those enrichment shape functions associated with the null space of the stiffness matrix. Numerical experiments indicate that the *XFEM-t* scheme, with the new tip enrichment, achieves the optimal  $O(h^2)$  convergence rate we expect of the underlying piece-wise linear FEM discretization, which is superior to the enrichment functions currently available in the literature for  $\frac{1}{2} < \lambda < 1$ . The *XFEM-s* scheme, with only signum enrichment to represent the crack geometry, achieves an  $O(h)$  convergence rate. It is also demonstrated that the standard  $P \rightarrow W$  formulation, based on the variational principle of minimum potential energy, is not suitable for modeling hydraulic fractures in which the fluid and the fracture fronts coalesce, while the mixed hybrid  $P\&W$  formulation based on the Hellinger-Reissner variational principle does not have this disadvantage.

*Keywords:* XFEM, Hydraulic Fractures, Convergence, Tip Enrichment

---

## 1. Introduction

Hydraulic fractures are brittle fractures that are induced to propagate in pre-stressed solid media due to the injection of a viscous fluid. These fractures occur both naturally due to buoyant magma flow [3, 4, 5, 6, 7, 8] or turbulent flooding under ice sheets [9] and glacier beds [10] or are deliberately engineered for a variety of industrial applications such as: the remediation of contaminated soils [11, 12, 13], waste disposal [14], to weaken the rock to sustain the block-caving process in mining [15, 16], however the most ubiquitous industrial application is the generation of HF in the oil and gas industry to enhance the recovery of hydrocarbons by creating permeable pathways [17, 18, 19].

The application to hydrocarbon extraction has intensified considerably in the last decade with the generation of HF from horizontal wells to extract natural gas from low permeability shales. The complex mechanics of this heterogeneous, anisotropic, ductile host rock that typically has extensive natural fractures poses considerable challenges to numerical modeling efforts aimed at simulating propagating HF in this complex environment. Even assuming a homogeneous, isotropic, elastic host rock, modeling hydraulic fracture propagation is complex, involving the solution of a system of degenerate, hypersingular integro-partial differential equations along with a singular free

boundary problem. For the latter host rock, a boundary integral formulation of the elasticity problem is the most efficient numerical scheme, which has enjoyed considerable development [20, 21, 22, 23, 24, 25, 26, 27]. However, if there is a need to model multiple, arbitrarily oriented, fractures propagating in host rock that comprises more complexity than a layered elastic material, then other methods such as the Finite Element Method (FEM) are advantageous.

Unfortunately, the prohibitive re-meshing cost of tracking a propagating fracture has hampered the development of Finite Element Methods [28, 29] for modeling propagating HF. However, the XFEM [30, 31, 32] holds much promise for the efficient numerical modeling of propagating HF within the FEM paradigm. In the XFEM methodology, the fracture is represented by augmenting the space of shape functions by specialized enrichment functions that are able to reproduce the discontinuous and singular elastic fields associated with the crack. These enrichment functions are restricted to elements in the vicinity of the fracture and its tips, while field variables in the bulk of the solid medium can be represented by standard polynomial basis functions. Thus fracture propagation can be captured even on a structured mesh by dynamically adjusting the enrichment process to incorporate the location of the moving fracture tips. Early applications of the XFEM to model HF propagation [33, 34] had focused on propagating so-called dry cracks in which the effect of fluid viscosity is not taken into account so that no solid-fluid coupling is required and the classic square-root enrichment functions from the linear elastic fracture mechanics can be used. It was not until the two recent papers [1, 2] that modeling the fully-coupled HF propagation problem was fully addressed and robust techniques were established to dynamically locate the singular free boundary. Moreover, the classic square-root enrichment is not adequate to represent the multiscale behavior of the width field encountered in HF. Indeed, for HF the width field behaves as  $w \sim \hat{s}^\lambda$  for  $\hat{s} \rightarrow 0$ , where  $\hat{s}$  is the distance to the crack tip, and  $\lambda : 1/2 \leq \lambda < 1$  varies according to the propagation regime determined by the dominant physical process active at that time [35]. HF enrichment functions suitable for a generalized power law index  $\lambda$  within this range have been presented [36] and numerical results were provided for a static crack for both the toughness asymptote  $\lambda = \frac{1}{2}$  and the viscous asymptote  $\lambda = \frac{2}{3}$  [37]. However numerical experiments indicate that these enrichment functions do not enable the XFEM to recover the optimal  $O(h^2)$  convergence rate of the piecewise linear discretization of the underlying FEM mesh. Therefore one objective of this paper is to derive the

appropriate enrichment functions for this general power law. We test these novel enrichment functions in a convergence study with  $\lambda = 2/3$ , in which we demonstrate that we are able to recover the optimal  $O(h^2)$  convergence rate. If enrichment is applied to all the nodes of tip-enriched elements, then the resulting XFEM stiffness matrix is singular due to a linear dependence among the enrichment shape functions. Fries [38] has shown how to eliminate this problem for the case of the classic toughness asymptote  $\lambda = \frac{1}{2}$ . In this paper we show how to remove this rank deficiency for the more general set of enrichment functions  $1/2 \leq \lambda < 1$  by eliminating those enrichment shape functions associated with the null space of the stiffness matrix.

In HF simulations the XFEM is used to repeatedly solve a suitable boundary value problem accounting for the deformation of the solid medium due to the pressurization of the crack. Typically boundary integral methods are used in HF models to solve this boundary value problem in the form of the Dirichlet to Neumann map between the crack opening displacement (or, fracture width) and the fluid pressure on the crack faces. While the boundary integral methods rely on specialized Green's functions for this representation, the XFEM does not provide an accurate representation of this mapping as it amounts to numerical differentiation of the displacements in order to determine stresses. Thus in HF simulations the XFEM is best suited to providing the Neumann to Dirichlet map between the prescribed fluid pressures applied to the crack faces and the deformation of the solid medium in the form of the crack opening displacement. The specific formulation of this Neumann to Dirichlet map that is required depends on whether the fluid front is distinct from the fracture front, in which case the HF develops a fluid lag, or the fluid and fracture fronts coalesce, in which case the net pressure field is singular at the crack tip (see [39]). If an HF develops a fluid lag, then the fracture tip is fluid-free and is characterized by a finite net pressure. In this case we can prescribe the net pressure along the entire crack and the XFEM is only required to determine the crack opening displacement, i.e. a standard Neumann to Dirichlet map. However, if the two fronts coalesce, then the singular net pressure at the crack tip requires special treatment. If we were to proceed as before and prescribe the pressure field over the entire crack, then the singular tip pressure can only be accurately determined in the form of an asymptotic that has a vanishingly small region of validity. On the other hand, the region of validity of an asymptotic expression for the crack width typically extends to 10% of the fracture length from the crack tip. Hence a more robust approach in this case is to formulate the boundary condition

in the elastic part of the problem by prescribing an asymptotic expression for the (finite) crack width in the crack tip, and the (finite) net pressure in the interior region of the crack away from the tips (in the so-called *channel region*). With this mixed formulation we are still using the XFEM to determine the Neumann to Dirichlet map within the channel region, which encompasses the majority of the crack.

During the development of the fully coupled XFEM schemes applicable to both fluid lag and coalescent front situations [1, 2] we identified two key boundary value problems that need to be solved repeatedly during the modeling of a propagating HF using the XFEM. In this paper we focus on determining the accuracy and convergence performance of the XFEM when used to solve these two types of boundary value problems, which are stated as follows:

- (I)  $P \rightarrow W$  (Neumann to Dirichlet map): given a prescribed pressure  $p$  (possibly having a power-law singularity at the crack tips) determine the crack opening displacement  $w$ , and
- (II)  $P\&W$  (Mixed): given the crack opening displacement  $w_t$  in a neighborhood  $\Sigma_t$  of the crack tip and the prescribed pressure  $p_c$  in the interior of the crack  $\Sigma_c = \Sigma \setminus \Sigma_t$ , where  $\Sigma$  denotes the crack surface, determine the crack opening displacement  $w$  along  $\Sigma_c$ .

To solve the boundary condition of type (I,  $P \rightarrow W$ ) above, it is straightforward to use the classical XFEM formulation based on the variational principle of the minimum of the potential energy. To solve the boundary condition of type (II,  $P\&W$ ), we use a new  $P\&W$  scheme which is a modification of the mixed hybrid XFEM presented by [40]. This formulation is based on the Hellinger-Reissner variational principle and requires a special enrichment to represent the stress, in addition to the enrichment tailored to represent the power law displacement field. In this paper we show that with the appropriate stress and displacement enrichment, the mixed hybrid  $P\&W$  formulation is superior to the classical  $P \rightarrow W$  XFEM formulation. Recall that the  $P\&W$  formulation is required in the context of a coupled model for a propagating HF in which fracture and fluid fronts coalesce.

While the XFEM achieves considerable savings over the FEM by avoiding the costly re-meshing process and recalculation of the large parts of the stiffness matrix, the numerical integration of the singular enrichment functions

that is required to determine the corresponding elements of the stiffness matrix can still be costly. These stiffness matrix elements have to be updated for each new trial position of the fracture front. Thus inspired by the weak-form tip asymptotics used for modeling HF with displacement discontinuity (DD) boundary elements [27], the so-called *XFEM-s* scheme for HF was developed [2]. In this scheme the singular tip enrichment is replaced by imposing the tip asymptotic behavior in a weak-sense and only the non-singular discontinuous sign enrichment functions required to represent the crack are used. Not only does this scheme avoid the costly numerical integration of singular functions, but the weak-form imposition of the tip asymptotics allows for multiple intra-element tip advances without requiring that the stiffness matrix be updated. Thus the *XFEM-s* scheme provides an efficient alternative to a crack-tip enriched XFEM within a coupled XFEM-based HF simulator. Naturally, this computational saving comes at the cost of accuracy, since the implementation of no tip enrichment is certainly sub-optimal. Thus another objective of this paper is to establish the spatial accuracy and convergence rate of the *XFEM-s* scheme when used to solve the two classes of boundary value problems (I) and (II), in order to provide useful information for the design of simulators based on this formulation.

In section 2, we describe the governing equations. In section 3, we present the weak formulations for the XFEM to solve the two types of the boundary conditions above. In section 4 we describe the enrichment strategy, and in section 5 we derive the new singular tip enrichment for a general crack width power law and for discretizations in which the stiffness matrix is singular, we demonstrate how to eliminate those enrichment shape functions associated with the stiffness matrix null space. Finally, in section 6 we study the performance and convergence of the  $P \rightarrow W$  and  $P\&W$  XFEM formulations with the new tip enrichment and without any tip enrichment, in the context of fluid driven crack modeling.

## 2. Problem formulation

### 2.1. Plane strain model

Consider a hydraulic fracture in an impermeable elastic medium in a state of plane strain whose stiffness is characterized by the Young's modulus  $E$  and the Poisson's ratio  $\nu$  (see figure 1). The fracture is assumed to be driven by the injection of a viscous fluid from a point source. In two dimensions, the fracture geometry is represented by a curve  $\Sigma$ ; a curvilinear coordinate  $s$  is

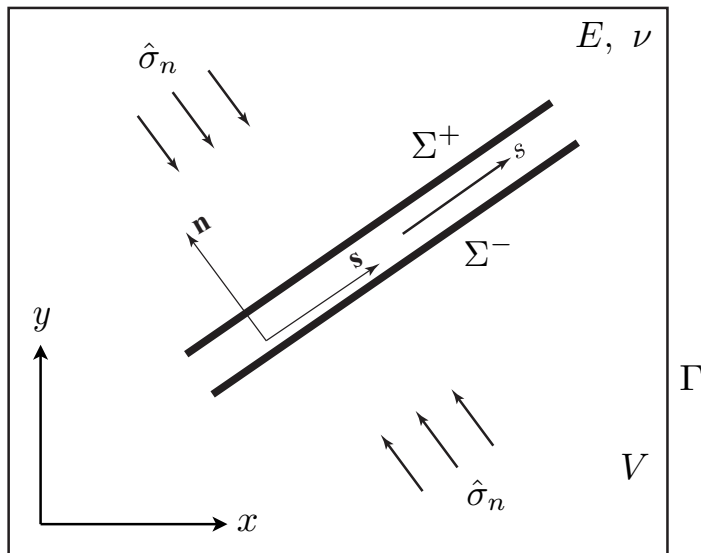


Figure 1: This figure represents a hydraulic fracture  $\Sigma$  within the solid medium occupying the region  $V$  with boundary  $\Gamma$ . The fracture depicted is assumed to be subject to a normal confining stress  $\hat{\sigma}_n$  only and no shear stress. The origin of the curvilinear coordinate  $s$  is located at the fluid source.

introduced along  $\Sigma$ , with the origin  $s = 0$  located at the fluid source. The medium is additionally assumed to be subjected to a uniform stress state (such as the ambient geological confining stress field) that can equivalently be represented by normal and shear tractions applied along the crack, denoted by  $\hat{\sigma}_n$  and  $\hat{\sigma}_s$ . This stress field naturally satisfies the equilibrium equation (4) below with a zero body force vector. In the present paper we consider a static fracture configuration for our convergence studies, in which the time variable is not involved and we do not specify any properties of the viscous fluid or the injection rate. Thus we focus on the solution of the solid mechanics part of the problem for which the XFEM is the key component. For brevity we do not discuss the lubrication component of the problem, coupling of the XFEM and the discretizations of the lubrication equation, or strategies to locate the singular free boundary. For details of this the reader is referred to [1, 2].

In HF simulations it is typically required that we construct a mapping between the crack width  $w(s)$  and the *net* pressure  $p(s) = p_f(s) - \hat{\sigma}_n(s)$ , in which  $p_f(s)$  is the fluid pressure along the crack faces. Two types of boundary conditions along the fracture are considered below, that complete the elastic

boundary value problem (BVP):

- (I)  $P \rightarrow W$  (Neumann to Dirichlet map): given a prescribed pressure  $p_n(s)$  along  $\Sigma$ , determine the crack opening displacement  $w(s)$  for  $s \in \Sigma$ ,

$$p(s) = p_n(s), \quad s \in \Sigma \quad (1)$$

- (II)  $P\&W$  (mixed: interior Neumann to Dirichlet, prescribed tip widths): given the crack opening displacement  $w_t(s)$  in a neighborhood  $\Sigma_t$  of the crack tip and the prescribed pressure  $p_c(s)$  in the interior of the crack (channel)  $\Sigma_c = \Sigma \setminus \Sigma_t$ , determine the crack opening displacement  $w(s)$  along  $\Sigma_c$ ,

$$w(s) = w_t(s), \quad s \in \Sigma_t; \quad p(s) = p_c(s), \quad s \in \Sigma_c \quad (2)$$

These two sets of boundary conditions lead to different XFEM implementations.

Finally, throughout the paper it is convenient to employ the notation  $E'$  for the plane strain modulus, defined by

$$E' = \frac{E}{1 - \nu^2} \quad (3)$$

## 2.2. Governing equations

The displacement field  $\mathbf{u}$  and the stress field  $\boldsymbol{\sigma}$  in the domain are defined with respect to the Cartesian coordinate system  $(x, y)$  and are represented by the components  $u_i$  and  $\sigma_{ij}$ , respectively. The equilibrium equation, for a body force field  $\mathbf{f}$  per unit volume, and Hooke's law for the linear elastic medium can be written in the following tensor form

$$\nabla \cdot \boldsymbol{\sigma} + \mathbf{f} = \mathbf{0} \quad (4)$$

$$\boldsymbol{\sigma} = \mathcal{C} : \boldsymbol{\varepsilon}(\mathbf{u}) \quad (5)$$

in which  $\mathcal{C}$  is the tensor of elastic constants, and  $\boldsymbol{\varepsilon}(\mathbf{u})$  is the strain tensor associated with the displacement  $\mathbf{u}$ ,

$$\boldsymbol{\varepsilon}(\mathbf{u}) = \frac{1}{2} \left( \nabla \mathbf{u} + (\nabla \mathbf{u})^T \right) \quad (6)$$

The domain is denoted by  $V$ , while its outer boundary is denoted by  $\Gamma$ , and the fracture surface is denoted by  $\Sigma$  (see figure 1). At the outer boundary  $\Gamma$ , the displacement is assumed to be given by a known function  $\mathbf{g}(x, y)$ ,

$$\mathbf{u}|_{\Gamma} = \mathbf{g} \quad (7)$$

To complete Eqs. (4) - (7), it is necessary to specify the boundary conditions along the crack. In order to do this, the two crack faces are identified as  $\Sigma^+$  and  $\Sigma^-$ , and the values of the displacement and the stress along each face are denoted by  $\mathbf{u}^+$  and  $\mathbf{u}^-$  and by  $\boldsymbol{\sigma}^+$  and  $\boldsymbol{\sigma}^-$ , respectively. The unit normal and tangent vectors along the crack are denoted by  $\mathbf{n}$  and  $\mathbf{s}$ , respectively, and are oriented as shown in figure 1. This definition of  $\mathbf{n}$  and  $\mathbf{s}$  is consistent with the outward normal direction for the crack face  $\Sigma^-$ .

The crack width is defined as the normal displacement jump at a point  $s$  along the crack,

$$w(s) = [[\mathbf{u}]]_{\Sigma} \cdot \mathbf{n} = (\mathbf{u}^+ - \mathbf{u}^-) \cdot \mathbf{n} \quad (8)$$

The normal and shear tractions are assumed to be continuous across the crack. The normal traction  $\sigma_n$  is equal to the net pressure (but opposite in sign), and the shear traction  $\sigma_s$  is equal to the applied shear stress. These constraints result in the conditions:

$$\sigma_n^+ = \sigma_n^- = -p(s) \quad (9)$$

$$\sigma_s^+ = \sigma_s^- = \hat{\sigma}_s(s) \quad (10)$$

Here the superscript  $+$  or  $-$  again denotes the crack face along which the stress component is computed. The normal and the shear tractions are obtained from the stress tensor as  $\sigma_n^{\pm} = \mathbf{n}^T (\boldsymbol{\sigma}^{\pm} \cdot \mathbf{n})$  and  $\sigma_s^{\pm} = \mathbf{s}^T (\boldsymbol{\sigma}^{\pm} \cdot \mathbf{n})$ .

In the above equations, the net pressure  $p(s)$  and the crack width  $w(s)$  cannot be prescribed simultaneously at the same point  $s$  on the crack. If one of these quantities is given, the other one has to be found from the solution to the elastic BVP. We consider the two BVPs in which equations (4) - (10) are complemented by the two types of the boundary conditions on the crack (in the normal direction): (1) or (2).

### 3. Weak formulation

#### 3.1. $P \rightarrow W$ scheme

Following [38] the domain  $V$  is discretized into a finite element mesh comprising a set of non-overlapping quadrilateral elements. The displacement in

$V$  is approximated by elements of the trial space  $\mathcal{U}_{\mathbf{u}}^h = \{\mathbf{u}^h \mid \mathbf{u}^h \in U, \mathbf{u}^h = \mathbf{g} \text{ on } \Gamma\}$  while variations are taken from the test space  $\mathcal{V}_{\mathbf{u}}^h = \{\mathbf{v}^h \mid \mathbf{v}^h \in U, \mathbf{v}^h = \mathbf{0} \text{ on } \Gamma\}$ . Here  $U$  is a finite-dimensional subspace of the Sobolev space  $H^1(V \setminus \Sigma) \times H^1(V \setminus \Sigma)$  that consists of the shape functions representing the discretization  $\mathbf{u}^h$  and which will be defined in Section 4. The domain  $V$  includes the crack  $\Sigma$ . The domain  $V \setminus \Sigma$  that does not contain the crack is assumed to be piecewise Lipschitz. The test and trial functions are assumed to be discontinuous at the crack  $\Sigma$  in a direction normal to the crack.

For a test function  $\mathbf{u}^h$  that is represented by a linear combination of shape functions, the corresponding strain  $\boldsymbol{\varepsilon}(\mathbf{u}^h)$  can be computed from (6), while the corresponding stress can be obtained from Hooke's law (5) to yield  $\boldsymbol{\sigma}(\mathbf{u}^h) = \mathcal{C} : \boldsymbol{\varepsilon}(\mathbf{u}^h)$ . The discretized weak formulation of the elasticity problem (1) and (4) - (10) seeks to find  $\mathbf{u}^h \in \mathcal{U}_{\mathbf{u}}^h$  such that

$$0 = \int_{V \setminus \Sigma} \boldsymbol{\varepsilon}(\mathbf{v}^h) : \boldsymbol{\sigma}(\mathbf{u}^h) dV - \int_{V \setminus \Sigma} \mathbf{v}^h \cdot \mathbf{f} dV + \int_{\Sigma} [[\mathbf{v}^h]] \cdot (-p_n \mathbf{n} + \hat{\sigma}_s \mathbf{s}) ds \quad (11)$$

for all  $\mathbf{v}^h \in \mathcal{V}_{\mathbf{u}}^h$ . In the above,  $[[\mathbf{v}]] = (\mathbf{v}^+ - \mathbf{v}^-)$  denotes the jump of  $\mathbf{v}$  across the crack.

Eq. (11) corresponds to the classical variational formulation obtained by setting the first variation of the potential energy functional to zero [41, 42],

$$\delta \Pi(\mathbf{u}, \delta \mathbf{u}) = 0 \quad (12)$$

$$\Pi(\mathbf{u}) = \int_{V \setminus \Sigma} \left[ \frac{1}{2} \boldsymbol{\sigma}(\mathbf{u}) : \boldsymbol{\varepsilon}(\mathbf{u}) - \mathbf{f} \cdot \mathbf{u} \right] dV + \int_{\Sigma} (-p_n \mathbf{n} + \hat{\sigma}_s \mathbf{s}) \cdot [[\mathbf{u}]] ds \quad (13)$$

in which  $\delta \mathbf{u}$  is the variation of the displacement in  $V$ . The first two terms in (13) represent the strain energy and the negative of the work of the body force on the displacement. The last term represents the negative of the work of the applied tractions on the displacement along the crack faces:

$$- \int_{\Sigma^+} (-p_n \mathbf{n}^+ + \hat{\sigma}_s \mathbf{s}^+) \cdot \mathbf{u}^+ ds - \int_{\Sigma^-} (-p_n \mathbf{n}^- + \hat{\sigma}_s \mathbf{s}^-) \cdot \mathbf{u}^- ds \quad (14)$$

### 3.2. *P&W Scheme*

We use the localized mixed hybrid formulation introduced in [40] to specify the normal displacement jump  $w_t$  along that part of the domain which is adjacent to the crack boundary  $\Sigma_t$ , and follow the formulation similar to that in the  $P \rightarrow W$  scheme for the rest of the domain. The domain  $V$  is discretized into a mesh  $\mathcal{F}$  of non-overlapping quadrilateral elements  $e$  each of which occupies the region  $V_e^h$ , such that:  $V = \bigcup_{e \in \mathcal{F}} V_e^h$ . The subset of elements that overlap with that part of the crack  $\Sigma_t$  along which  $w_t$  is prescribed is denoted  $\mathcal{B}$ :  $\mathcal{B} = \{e \in \mathcal{F} : V_e^h \cap \Sigma_t \neq \emptyset\}$ . The domain  $V$  is thus artificially partitioned into two domains:  $V_o$  and  $V_* = \bigcup_{e \in \mathcal{B}} V_e^h$ , where  $V_o = V \setminus V_*$  contains all elements that do not overlap with  $\Sigma_t$  (See Fig. 2). Hence, the domain  $V_o$  overlaps with the channel region of the crack,  $\Sigma_c$ ; the domain  $V_*$  overlaps with the channel  $\Sigma_c$  and the tip region  $\Sigma_t$ . The boundary  $\partial V_*$  of the domain  $V_*$  is the interface between  $V_o$  and  $V_*$ .

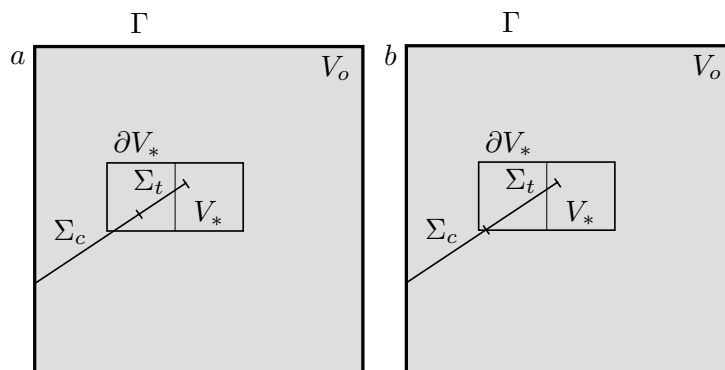


Figure 2: Domain decomposition  $V = V_o \cup V_*$  for the *P&W* scheme. In the depicted example, only one crack tip is situated within the computational domain  $V$ ; the subdomain  $V_*$  consists of two quadrilateral finite elements shown, that comprise the set  $\mathcal{B}$ . The channel-tip boundary is inside an element (a) or at the edge of a finite element (b).

As in the  $P \rightarrow W$  scheme above, the displacement in  $V$  is approximated by elements of the trial space  $\mathcal{U}_{\mathbf{u}}^h = \{\mathbf{u}^h \mid \mathbf{u}^h \in U, \mathbf{u}^h = \mathbf{g} \text{ on } \Gamma\}$  while variations are taken from the test space  $\mathcal{V}_{\mathbf{u}}^h = \{\mathbf{v}^h \mid \mathbf{v}^h \in U, \mathbf{v}^h = \mathbf{0} \text{ on } \Gamma\}$ . Again,  $U$  is a finite-dimensional subspace of the Sobolev space  $H^1(V \setminus \Sigma) \times H^1(V \setminus \Sigma)$  that consists of the shape functions representing the discretization  $\mathbf{u}^h$  and which will be defined in Section 4. The domain  $V \setminus \Sigma$  that does not contain the crack  $\Sigma$  is assumed to be piecewise Lipschitz. The test and trial functions

are assumed to be discontinuous at the crack  $\Sigma$  in a direction normal to the crack.

For a test or trial function  $\mathbf{u}^h$ , the corresponding strain  $\boldsymbol{\varepsilon}(\mathbf{u}^h)$  is computed from (6), while the corresponding stress can be obtained from Hooke's law (5) to yield  $\boldsymbol{\sigma}(\mathbf{u}^h) = \mathcal{C} : \boldsymbol{\varepsilon}(\mathbf{u}^h)$ . However, in each element  $e \in \mathcal{B}$ , the stress  $\boldsymbol{\sigma}$  is introduced as an auxiliary tensor variable for which Hooke's law (5) is weakly imposed. Following [40] we approximate  $\boldsymbol{\sigma}$ , by introducing the test (and trial) tensor function space

$$\mathcal{S}_{\boldsymbol{\sigma}}^h = \{ \boldsymbol{\sigma}^h \mid \sigma_{ij}^h = \sigma_{ji}^h, \sigma_{ij}^h \in H^{-1h} \text{ for } i = 1, 2 \text{ and } j = 1, 2 \}$$

in which  $H^{-1h}$  is a finite-dimensional subspace of the space of functions that are square-integrable in each element in  $\mathcal{B}$  and which are discontinuous at the element edges and at the crack  $\Sigma$  in a direction normal to the crack. In Section 4 we define the shape functions for this subspace on the element level for each  $e \in \mathcal{B}$ .

The discretized weak formulation of the elasticity problem (2) and (4) - (10) seeks to find  $(\mathbf{u}^h, \boldsymbol{\sigma}^h) \in \mathcal{U}_{\mathbf{u}}^h \times \mathcal{S}_{\boldsymbol{\sigma}}^h$  such that, for all  $(\mathbf{v}^h, \boldsymbol{\tau}^h) \in \mathcal{V}_{\mathbf{u}}^h \times \mathcal{S}_{\boldsymbol{\sigma}}^h$ ,

$$0 = \int_{V_o \setminus \Sigma} \boldsymbol{\varepsilon}(\mathbf{v}^h) : \boldsymbol{\sigma}(\mathbf{u}^h) dV + \int_{\Sigma_c} [[\mathbf{v}^h]] \cdot (-p_c \mathbf{n} + \hat{\sigma}_s \mathbf{s}) ds \quad (15)$$

$$+ \sum_{e \in \mathcal{B}} \int_{V_e^h \setminus \Sigma} [\boldsymbol{\varepsilon}(\mathbf{v}^h) : \boldsymbol{\sigma}^h + \boldsymbol{\tau}^h : (\boldsymbol{\varepsilon}(\mathbf{u}^h) - \mathcal{C}^{-1} : \boldsymbol{\sigma}^h)] dV \quad (16)$$

$$- \int_{V \setminus \Sigma} \mathbf{v}^h \cdot \mathbf{f} dV + \sum_{e \in \mathcal{B}} \int_{\Sigma_{t,e}} ([[ \mathbf{v}^h ]]) \cdot \mathbf{s} \hat{\sigma}_s ds \quad (17)$$

$$+ \sum_{e \in \mathcal{B}} \int_{\Sigma_{t,e}} [([[\mathbf{v}^h]]) \cdot \mathbf{n}] (\mathbf{n} \cdot \{ \boldsymbol{\sigma}^h \} \cdot \mathbf{n}) + (\mathbf{n} \cdot \{ \boldsymbol{\tau}^h \} \cdot \mathbf{n}) ([[\mathbf{u}^h]] \cdot \mathbf{n} - w_t)] ds \quad (18)$$

where  $\Sigma_{t,e} = \Sigma_t \cap V_e^h$ ,  $\{ \cdot \}$  denotes the averaged quantity obtained from the two crack faces  $\Sigma^\pm$ , i.e.,  $\{ \boldsymbol{\sigma} \} = \frac{1}{2} (\boldsymbol{\sigma}^+ + \boldsymbol{\sigma}^-)$ , and  $[[\mathbf{v}]] = (\mathbf{v}^+ - \mathbf{v}^-)$  denotes the jump of  $\mathbf{v}$  across the crack.

The above weak form (15) - (18) can be obtained by multiplying Eqs. (2) and (4) - (10) by arbitrary functions of suitable dimensions, integrating the result over the corresponding domains and boundaries and using integration by parts, following the derivation in [40]. Alternatively, this weak form can

be obtained by setting to zero the first variation of a mixed hybrid potential that includes the potential energy functional for the domain  $V_o$ , the hybrid Hellinger-Reissner potential [43, 44, 45, 46] for the domain  $V_*$ , and an interface potential that enforces the continuity of the solution across  $\partial V_*$  (see Appendix A for details).

From a mathematical point of view the weak form (15)-(18) allows the transition from one of the boundary conditions in (2) to the other to occur within a single element. However, in numerical experiments we observed a reduction in accuracy when both types of the boundary conditions (2) are present in one finite element, i.e. when in a single finite element one has to compute integrals over  $\Sigma_c$  and  $\Sigma_t$  in (15) - (18). Thus we avoid switching the imposed boundary condition within one element by choosing to impose only one of the two conditions from (2) in each finite element cut by the crack. This is achieved by ensuring that the boundary between the channel  $\Sigma_c$  and the tip  $\Sigma_t$  falls at the edge of a finite element, as shown in Fig. 2b. As a result, the elements in the tip zone  $V_*$  do not intersect with the channel, i.e.  $\Sigma_c \cap V_e^h = \emptyset$  for all  $e \in \mathcal{B}$ . Therefore, all numerical results in this paper were obtained under this constraint.

## 4. Shape functions spaces: sign and fixed radius tip enrichment

### 4.1. Displacement enrichment

The fundamental idea behind the XFEM is to efficiently represent interfaces and cracks by augmenting the standard set of Lagrange shape functions by specialized enrichment functions in the elements around these features. Following [38] cracks are represented by two forms of enrichment, namely sign and tip enrichment, as originally suggested by [30]. Sign enrichment is necessary to define the geometry of the crack while the tip enrichment is required to restore the order of convergence expected of the underlying finite element discretization of the elasticity problem, which degrades due to the presence of the singular behavior at the crack tips. Sign enrichment is relatively inexpensive compared to tip enrichment, which requires computationally intensive spatial integration of the singular enrichment functions in tip-enriched elements. In this paper we will consider the accuracy and convergence properties of the  $P \rightarrow W$  and  $P\&W$  XFEM schemes for modeling hydraulic fractures, with and without tip enrichment. The details of the two enrichments are as follows:

- (I) Sign enrichment: the crack geometry is defined by enriching those elements that intersect the crack by the sign function defined as follows:

$$\mathbf{sg}(\mathbf{x}) = \text{sign}(\phi(\mathbf{x})), \quad \mathbf{x} \in V \quad (19)$$

in which  $\phi(\mathbf{x}) = \pm \min_{\tilde{\mathbf{x}} \in \tilde{\Sigma}} |\mathbf{x} - \tilde{\mathbf{x}}|$  is the signed distance function that has different signs on the two sides of the crack or its extension  $\tilde{\Sigma}$ . The curve  $\tilde{\Sigma}$  includes the crack and may extend beyond each crack tip in the direction tangential to the crack to the farthest edge of the encompassing finite element, for the XFEM without tip enrichment.

- (II) Tip enrichment: singular behavior at the crack tip is captured by introducing specialized enrichment basis functions that are obtained from special solutions of the elastic equilibrium equations. Motivated by applications to HF in this paper we consider the following general class of power-law tip asymptotic behavior of the width field in the limit as the distance  $\hat{s}$  to the fracture tip tends to zero:

$$w_t(\hat{s}) \stackrel{\hat{s} \rightarrow 0}{\sim} A \hat{s}^\lambda, \quad \text{where} \quad \frac{1}{2} \leq \lambda < 1, \quad (20)$$

for some constant  $A$ . This asymptote includes the limiting toughness dominated ( $\lambda = \frac{1}{2}$ ) and viscosity dominated ( $\lambda = \frac{2}{3}$ ) regimes. It can be shown by local analysis of the tip asymptotics [47] that the corresponding pressure behavior is of the form  $p_t \stackrel{\hat{s} \rightarrow 0}{\sim} \frac{1}{4} A \lambda \cot(\pi \lambda) \hat{s}^{\lambda-1}$  when  $\frac{1}{2} < \lambda < 1$ . Consistent with this asymptotic behavior, the appropriate enrichment basis functions for the displacement and corresponding stress fields are obtained in the following section. They are of the form:

$$\begin{aligned} \boldsymbol{\psi}^{\mathbf{u},\lambda} &= r^\lambda \{ \sin(\lambda\theta), \cos(\lambda\theta), \sin(\lambda-2)\theta, \cos(\lambda-2)\theta \} \\ \boldsymbol{\psi}^{\boldsymbol{\sigma},\lambda} &= r^{\lambda-1} \{ \sin(\lambda-1)\theta, \cos(\lambda-1)\theta, \sin(\lambda-3)\theta, \cos(\lambda-3)\theta \} \end{aligned} \quad (21)$$

where  $(r, \theta)$  are polar coordinates centered at the fracture tip, so that the values  $\theta = \pm\pi$  correspond to the two crack faces. The tip enrichment comprises the four singular functions  $\{\psi_j^{\mathbf{u}}\}$  defined in (21) that are used to represent the singular behavior at the fracture tips.

For the XFEM with tip enrichment, which we refer to as the *XFEM-t* scheme, we define the set  $I_t$  of all nodes that are within a prescribed radius  $\rho$  from either crack tip  $\mathbf{x}_{tip}$ , i.e.,  $I_t = \{i \in I : |\mathbf{x}_i - \mathbf{x}_{tip}| \leq \rho\}$ , where  $\mathbf{x}_i \in V$  denote

coordinates of the finite element node  $i$ , and  $I$  is the set of all nodes. We also define the set  $I_s$  comprising all the nodes of the elements cut by the crack, excluding the nodes already in  $I_t$ , so that  $I_t \cap I_s = \emptyset$ .

The finite-dimensional Galerkin space  $U$ , to which the approximations of the displacement belong in the  $P \rightarrow W$  and  $P\&W$  schemes (Section 3), is defined by  $U = H^{1h} \times H^{1h}$  and is spanned by the following shape functions:

$$H^{1h} = \left\{ \sum_{i \in I} a_i N_i(\mathbf{x}) + R_s(\mathbf{x}) \sum_{i \in I_s^*} b_i N_i(\mathbf{x}) (\mathbf{sg}(\mathbf{x}) - \mathbf{sg}(\mathbf{x}_i)) + R_t(\mathbf{x}) \sum_{i \in I_t^*} N_i(\mathbf{x}) \sum_{j=1}^4 c_i^j (\psi_j^{\mathbf{u}}(\mathbf{x}) - \psi_j^{\mathbf{u}}(\mathbf{x}_i)) \right\} \quad (23)$$

where  $\mathbf{x} \in V \setminus \Sigma$ ;  $N_i$  are the standard piecewise bi-linear Lagrange basis functions; and  $a_i, b_i, c_i^j \in \mathbb{R}$ . Here  $I_s^*$  is the set of all nodes of elements that are cut by the crack *and* that have at least one node in  $I_s$ , and  $I_t^*$  is the set of all nodes in elements that have at least one node in  $I_t$ . Naturally,  $I_s \subseteq I_s^*$ ,  $I_t \subseteq I_t^*$ , and  $I_s^* \cap I_t^* \neq \emptyset$  provided  $I_t^* \neq \emptyset$ . As in a standard XFEM [48], the sign and tip enrichment functions in (23) are multiplied by the nodal Lagrange basis functions  $N_i$ , thus maintaining the partition of unity property sufficient for an optimal convergence rate [49]. However, in a standard XFEM [48], there is a loss of partition of unity in the blending elements that have both tip-enriched and non tip-enriched nodes, which results in a reduced accuracy or a sub-optimal convergence rate. To maintain the partition of unity property in the complete domain, which is sufficient to obtain an optimal convergence rate for the XFEM [50], special treatment is required for the blending elements [48]. We follow the ramp function approach of the corrected XFEM of Fries [38] and the blending strategy of Ventura et al. [51]. Singular tip enrichment is introduced at all nodes in  $I_t^*$ , and sign enrichment is introduced at all nodes in the set  $I_s^*$ . The two ramp functions  $R_t(\mathbf{x}) = \sum_{i \in I_t} N_i(\mathbf{x})$  and  $R_s(\mathbf{x}) = \sum_{i \in I_s} N_i(\mathbf{x})$  are introduced in (23) to blend the two enrichments.

For the XFEM without tip enrichment, which we refer to as the *XFEM-s* scheme, the crack geometry is defined only by the sign enrichment and the representation (23) is used with  $I_t^* = I_t = \emptyset$  and  $R_t(\mathbf{x}) = 0$ . The set  $I_s$  is defined for this case in a special way described below.

It should be noted that, for the XFEM without tip enrichment, the displacement shape functions (23) are discontinuous along the extended crack  $\tilde{\Sigma}$ , and the weak form (11) or (15) - (18) has to be reformulated for the extended

crack  $\tilde{\Sigma}$ . To keep a unified formulation of the XFEM schemes with different enrichment strategies and use the weak form (11) or (15) - (18) for either enrichment, in the following we use the notation  $\Sigma$  to denote the *extended* crack  $\Sigma = \tilde{\Sigma}$  for the XFEM without tip enrichment and the *actual* crack for the XFEM with tip enrichment. In particular, for the XFEM without tip enrichment, the line integrals in (17) and (18) in the element containing the crack tip are computed over the extended elemental tip region  $\Sigma_{t,e} = \Sigma_t \cap V_e^h$ , in which  $\Sigma_t$  is the crack tip region extended beyond the actual crack tip to the edge of the encompassing finite element, in the direction tangential to the crack. We refer to the intersection of the extended crack with that edge of the encompassing finite element as the “virtual” crack tip, and denote that part of the crack between the actual and the virtual crack tips as  $\bar{\Sigma}$  (see Fig. 3). However, all input data ( $w_t, \hat{\sigma}_s, p_n$ ) is set to zero beyond the actual crack tip along  $\bar{\Sigma}$ , i.e. the integrals of the prescribed displacement jump  $w_t$  in (18), of the prescribed shear traction in the tip  $\hat{\sigma}_s$  in (17) and in (11), and of the prescribed pressure in the tip  $p_n$  in (11) are computed over the actual crack (not the extended crack) for either enrichment strategy.

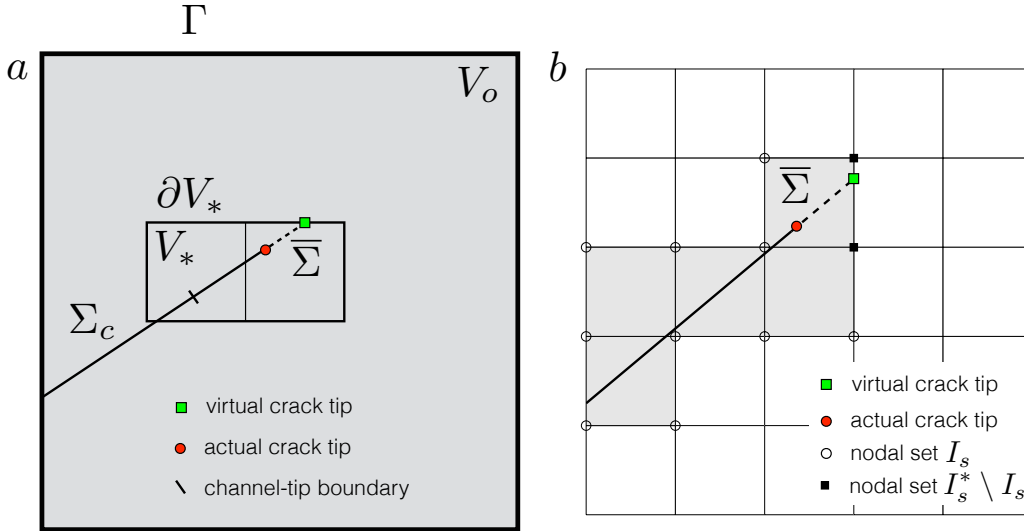


Figure 3: Structure of sign enrichment for XFEM without tip enrichment (*XFEM-s*): crack extension and virtual crack tip (a) and nodal set  $I_s$  (b).

As a result, for the XFEM without tip enrichment, the strong-form elastic problem that is obtained from the weak form (either (11) or (15) - (18)) extends the boundary condition applied in the tip element (given shear traction

$\hat{\sigma}_s$  and either given pressure  $p_n$  or given crack width  $w_t$ ) to that part  $\bar{\Sigma}$  of the crack between the actual and the virtual crack tips. This approximation is not equivalent to the original elastic problem defined in Section 2.2 in which the boundary condition on  $\bar{\Sigma}$  would be the continuity of the displacement,  $[[\mathbf{u}]]_{\bar{\Sigma}} = 0$ , if the crack was artificially extended beyond the actual crack tip. However, this discrepancy between the prescribed boundary data in the approximation and the continuity of the actual displacements is only limited to a portion  $\bar{\Sigma}$  of the tip element.

Further modifications of the XFEM without tip enrichment are possible in order to obtain the weak form with the boundary conditions on  $\bar{\Sigma}$  equivalent to the original elastic problem. For example, for the  $P \rightarrow W$  scheme, one may obtain the corresponding weak form from a hybrid variational principle [46] in which the traction vector on  $\bar{\Sigma}$  is introduced as an independent variable subject to variation, and an interface potential is added to the potential energy functional (13) to enforce the continuity condition  $[[\mathbf{u}]]_{\bar{\Sigma}} = 0$ . The same approach can be used for the  $P\&W$  scheme, in which such an interface potential for  $\bar{\Sigma}$  is added to the mixed hybrid Hellinger-Reissner potential (51) - (53) given in Appendix A. For the  $P\&W$  scheme it would result in evaluating the integrals of the prescribed displacement jump  $w_t$  in (18) and of the prescribed shear traction in the tip  $\hat{\sigma}_s$  in (17) over  $\Sigma_t \setminus \bar{\Sigma}$  and adding the integrals over  $\bar{\Sigma}$  that weakly enforce the continuity condition  $[[\mathbf{u}]]_{\bar{\Sigma}} = 0$  in the same way as it is done for the displacement jump boundary condition in the weak form obtained in [40]. These modifications are outside the scope of the present paper, which we leave for a subsequent investigation.

It should also be noted that the displacement shape functions (23) must be continuous across the interface  $\partial V_*$  to comply with the assumptions used to obtain the weak form (15) - (18) (see Appendix A). In particular, the displacement shape functions must be continuous across the finite element edge containing the virtual crack tip for the XFEM without tip enrichment. To achieve this, there must be no contribution from the sign enrichment to the displacement approximation in the finite element that does not contain the crack but contains the virtual crack tip. This can be done, for example, by excluding the two nodes on the edge containing the virtual crack tip from the sign enrichment (see Fig. 3), similar to the approach in [52]. The accuracy of this method depends on how the crack cuts the tip element (i.e. the type of cut in the tip element), since the crack width in this element is only enforced weakly via (18). However, we found that it can be more advantageous to use a ramp function approach that maintains the partition of unity property in

the tip element. Namely, for the XFEM without tip enrichment, we define the nodal set  $I_s$  for the sign enrichment as the set of all nodes of the elements cut by the crack, excluding the two nodes on the edge containing the virtual crack tip (Fig. 3). The set  $I_s^*$  then comprises all the nodes of the elements cut by the crack, and the ramp function  $R_s(\mathbf{x}) = \sum_{i \in I_s} N_i(\mathbf{x})$  ensures the continuity of the displacement approximation (23) across the edge containing the virtual crack tip. For the numerical example with  $\lambda = 2/3$  and the *P&W / XFEM-s* scheme presented in Section 6.2, this ramp-function approach provided higher convergence rates for the approximation errors than those obtained using the method in which either (a) no ramp function was used and all four nodes of the tip element were enriched with the sign enrichment - thus violating the continuity requirement across  $\partial V_*$ ; or (b) no ramp function was used and only two nodes of the tip element, that do not share the edge with the virtual crack tip, were enriched with the sign enrichment - thus satisfying the continuity requirement across  $\partial V_*$ . For the numerical examples presented in this paper, this ramp-function approach was used for the XFEM without tip enrichment. Note that this ramp function is not involved in the stress approximation within the XFEM without tip enrichment (see section 4.2).

Other research [53, 54, 55], which employed the sign enrichment to represent the complete crack, modified the enrichment strategy in the tip element so that the enrichment is only discontinuous up to the crack tip. For example, [53] used the sign enrichment multiplied by a smooth ramp function vanishing at the actual crack tip inside the element. These approaches [53, 54, 55] would be more accurate since they capture the exact location of the crack tip. However for a fully-coupled HF propagation model, these approaches would be less efficient than the present approach due to the following consideration.

Sign enrichment tailored to terminate exactly at the crack tip [53, 54, 55] or a modification of the weak form to weakly impose the continuous displacement beyond the actual crack tip, described above, are means to use the sign enrichment in the tip element while keeping a continuous displacement field ahead of the crack tip. In all of these approaches, the stiffness matrix needs to be updated each time when the crack tip moves, even if the movement is within a single finite element; the updated stiffness matrix needs to be inverted to get an updated solution to the XFEM linear system. In contrast, the present approach requires us to update the stiffness matrix only once when the crack tip moves into a single finite element. To give a specific example, we refer to our coupled ILSA-XFEM algorithm [2], in which for each step of a hydraulic fracture propagation the new location of the crack

front is found using the implicit level-set algorithm (ILSA). Within the ILSA scheme, several iterations of the crack-front may be required within a single finite element until convergence is reached. Further, the channel pressure  $p_c$  is represented by means of  $n$  shape functions in which  $n$  is roughly the number of finite elements cut by the crack; therefore each time the stiffness matrix is changed, the XFEM linear system has to be solved  $n$  times. The present approach, which only updates the stiffness matrix once per crack-tip finite element, offers clear computational savings for such an algorithm.

Thus we consider two enrichment schemes:

*The XFEM-s scheme:* we assume that only sign enrichment is used in all elements cut by the crack. In the elements containing the fracture tips, the sign enrichment extends in the fracture growth direction, beyond the actual tip of the fracture, to the farthest edge of the finite element. While the sign enrichment for this case actually extends beyond the tip to the far edge of the encompassing finite element, in this extended region it is assumed that all input data  $(w_t, \hat{\sigma}_s, p_n)$  is zero, so that there is no contribution from the prescribed boundary conditions to the weak form beyond the crack tip. In addition, the ramp function is used to cancel contributions of the sign enrichment at the finite element edge containing the virtual crack tip and to the element beyond the virtual crack tip.

*The XFEM-t scheme:* we assume that the sign enrichment covers only the channel elements and that crack tip enrichment is used for the tip elements according to (23). For the  $P\&W$  formulation, it is also assumed that blending of the two enrichments takes place in the channel, i.e. the tip enrichment radius  $\rho$  is chosen so that elements for which tip enrichment is applied completely cover the tip region  $\Sigma_t$ .

#### 4.2. Stress enrichment

In the  $P\&W$  scheme (Section 3.2), the stress in each element  $V_e^h$ ,  $e \in \mathcal{B}$ , is represented by the shape functions from the finite-dimensional space  $H^{-1h}$  defined on an element level as follows:

- For the  $XFEM-t$  scheme, we choose the radius of the tip enrichment  $\rho$  so that all nodes of the elements in the set  $\mathcal{B}$  are located within the distance  $\rho$  from the closest crack tip, i.e.  $\bigcup_{e \in \mathcal{B}} I_e \subset I_t$ , where  $I_e$  denotes the set of all nodes in element  $e$ . Hence the displacement shape functions (23) do not involve sign enrichment in the sub-domain  $\bigcup_{e \in \mathcal{B}} V_e^h$ ,

and the stress components can be represented by the four singular functions  $\{\psi_j^\sigma\}$  given in (22) and by standard Lagrange basis functions,

$$\begin{aligned}
H^{-1h} &= \left\{ \bigcup_{e \in \mathcal{B}} v^e(\mathbf{x}) : \right. \\
v^e(\mathbf{x}) &= \sum_{i \in I_e} a_i^e N_i(\mathbf{x}) + \sum_{i \in I_e} N_i(\mathbf{x}) \sum_{j=1}^4 c_i^{j,e} (\psi_j^\sigma(\mathbf{x}) - \psi_j^\sigma(\mathbf{x}_i)) \text{ if } \mathbf{x} \in V_e^h; \\
v^e(\mathbf{x}) &= 0 \text{ if } \mathbf{x} \notin V_e^h \left. \right\}
\end{aligned}$$

where  $\mathbf{x} \in \bigcup_{e \in \mathcal{B}} V_e^h \setminus \Sigma$ , and  $a_i^e, c_i^{j,e} \in \mathbb{R}$ .

- For the XFEM-s scheme the stress components are represented by the sign enrichment and by standard Lagrange basis functions,

$$\begin{aligned}
H^{-1h} &= \left\{ \bigcup_{e \in \mathcal{B}} v^e(\mathbf{x}) : \right. \\
v^e(\mathbf{x}) &= \sum_{i \in I_e} a_i^e N_i(\mathbf{x}) + \sum_{i \in I_e} b_i^e N_i(\mathbf{x}) (\text{sg}(\mathbf{x}) - \text{sg}(\mathbf{x}_i)) \text{ if } \mathbf{x} \in V_e^h; \\
v^e(\mathbf{x}) &= 0 \text{ if } \mathbf{x} \notin V_e^h \left. \right\}
\end{aligned}$$

where again  $\mathbf{x} \in \bigcup_{e \in \mathcal{B}} V_e^h \setminus \Sigma$ ;  $a_i^e, b_i^e \in \mathbb{R}$ ; and  $I_e$  denotes the set of all nodes in element  $e$ .

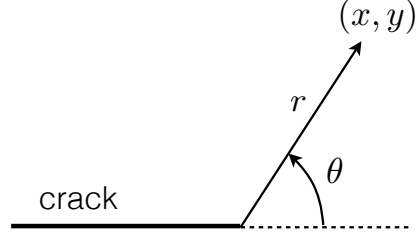
## 5. Singular tip enrichment for power-law crack tip

### 5.1. Asymptotic solution

Within the XFEM, a crack can be efficiently represented by augmenting the standard set of Lagrange shape functions by specialized enrichment functions in elements that are cut by the crack as well as the elements that are close to the crack tips. The crack tip enrichment is required to restore the order of convergence expected of the underlying finite element discretization of the elasticity problem, which degrades due to the presence of the singular behavior at the crack tips. Consistently with the classic LEFM, the displacement field at the tip of a brittle crack can be represented in XFEM using the following square root tip enrichment (e.g. [56, 57, 31, 38, 48]),

$$\boldsymbol{\psi}^u = r^{1/2} \{ \sin(\theta/2), \cos(\theta/2), \sin(\theta/2) \sin \theta, \cos(\theta/2) \sin \theta \} \quad (24)$$

Figure 4: Crack-tip polar coordinates.



where  $(r, \theta)$  are the polar coordinates centered at the fracture tip, so that the values  $\theta = \pm\pi$  correspond to the two crack faces (see Fig. 4). These functions span the dominant singularity in the displacement field in the asymptotic solution at the tip of a traction-free crack by Williams [58, 59, 42]. This enrichment basis is suitable for modeling hydraulic fractures propagating in the toughness regime [35], in which  $\lambda = \frac{1}{2}$ . However, when other physical processes are present, such as viscous dissipation or fluid leak-off, then power law behavior in the range  $\frac{1}{2} \leq \lambda < 1$  needs to be considered.

For a general power law width asymptote (20) with  $\frac{1}{2} \leq \lambda < 1$ , the crack-tip enrichment that spans the dominant singularity in the elastic solution can also be obtained using the stress function approach used by Williams [58, 59, 42]. In the absence of a body force, the stresses in the polar coordinate system  $(r, \theta)$  associated with the crack tip can be represented as

$$\sigma_{rr} = \frac{1}{r^2} \frac{\partial^2 U}{\partial \theta^2} + \frac{1}{r} \frac{\partial U}{\partial r} \quad (25)$$

$$\sigma_{\theta\theta} = \frac{\partial^2 U}{\partial r^2} \quad (26)$$

$$\sigma_{r\theta} = -\frac{\partial}{\partial r} \left( \frac{1}{r} \frac{\partial U}{\partial \theta} \right) \quad (27)$$

where  $U(r, \theta)$  is the Airy stress function that satisfies the biharmonic equation

$$\nabla^4 U = 0 \quad (28)$$

The strain components can be found from the stresses using Hooke's law, and the displacement can be obtained by integrating the strain.

We are seeking a solution of Eq. (28) that produces the displacement proportional to  $r^\lambda$  and stresses proportional to  $r^{\lambda-1}$ , according to the power-law tip asymptote for a power-law exponent  $\lambda$ . This solution has a general form [59, 42]

$$U = r^{\lambda+1} \{C_1 \sin(\lambda + 1)\theta + C_2 \cos(\lambda + 1)\theta + C_3 \sin(\lambda - 1)\theta + C_4 \cos(\lambda - 1)\theta\} \quad (29)$$

where four arbitrary constants are involved. Without loss of generality, we can assume that the crack is aligned with the  $x$ -axis. Hence the corresponding components of stress and displacement in the Cartesian coordinates  $(x, y)$  are found to be

$$\begin{aligned} \sigma_{11} &= r^{\lambda-1} \lambda \{ [2C_3 - C_1(1 + \lambda)] \sin(\lambda - 1)\theta + C_3(1 - \lambda) \sin(\lambda - 3)\theta \\ &\quad + [2C_4 - C_2(1 + \lambda)] \cos(\lambda - 1)\theta + C_4(1 - \lambda) \cos(\lambda - 3)\theta \}; \\ \sigma_{22} &= r^{\lambda-1} \lambda \{ [2C_3 + C_1(1 + \lambda)] \sin(\lambda - 1)\theta - C_3(1 - \lambda) \sin(\lambda - 3)\theta \\ &\quad + [2C_4 + C_2(1 + \lambda)] \cos(\lambda - 1)\theta - C_4(1 - \lambda) \cos(\lambda - 3)\theta \}; \\ \sigma_{12} &= r^{\lambda-1} \lambda \{ C_2(1 + \lambda) \sin(\lambda - 1)\theta - C_4(1 - \lambda) \sin(\lambda - 3)\theta \\ &\quad - C_1(1 + \lambda) \cos(\lambda - 1)\theta + C_3(1 - \lambda) \cos(\lambda - 3)\theta \}; \\ u_1 &= \frac{r^\lambda}{E'(1-\nu)} \{ [\kappa C_3 - C_1(1 + \lambda)] \sin(\lambda\theta) - \lambda C_3 \sin(\lambda - 2)\theta \\ &\quad + [\kappa C_4 - C_2(1 + \lambda)] \cos(\lambda\theta) - \lambda C_4 \cos(\lambda - 2)\theta \}; \\ u_2 &= \frac{r^\lambda}{E'(1-\nu)} \{ [\kappa C_4 + C_2(1 + \lambda)] \sin(\lambda\theta) + \lambda C_4 \sin(\lambda - 2)\theta \\ &\quad - [\kappa C_3 + C_1(1 + \lambda)] \cos(\lambda\theta) - \lambda C_3 \cos(\lambda - 2)\theta \} \end{aligned}$$

where  $\kappa = 3 - 4\nu$ .

By examining the terms involved in the above expressions for the displacement and stress, a basis comprising four functions can be identified that spans the representation of the solution in the vicinity of the crack tip. This basis for the displacement field in the Cartesian coordinates is given by

$$\boldsymbol{\psi}^{\mathbf{u},\lambda} = r^\lambda \{ \sin(\lambda\theta), \cos(\lambda\theta), \sin(\lambda - 2)\theta, \cos(\lambda - 2)\theta \} \quad (30)$$

and the corresponding basis for the stress field is

$$\boldsymbol{\psi}^{\boldsymbol{\sigma},\lambda} = r^{\lambda-1} \{ \sin(\lambda - 1)\theta, \cos(\lambda - 1)\theta, \sin(\lambda - 3)\theta, \cos(\lambda - 3)\theta \} \quad (31)$$

These bases can thus be used as the enrichment functions in the vicinity of the crack tip in XFEM, for a power-law exponent  $\lambda : \frac{1}{2} \leq \lambda < 1$ .

## 5.2. Discussion

*The new enrichment is equivalent to the classic enrichment when  $\lambda = 1/2$ .*

For the particular case of a LEFM asymptote at the crack tip (20) with  $\lambda = 1/2$ , the enrichment basis (30) is equivalent to the classic basis (24), since each function in the basis  $\boldsymbol{\psi}^{\mathbf{u},1/2}$  in (30) can be expressed as a linear combination of the functions in the basis  $\boldsymbol{\psi}^{\mathbf{u}}$  in (24), and, conversely, each function in the basis  $\boldsymbol{\psi}^{\mathbf{u}}$  can be expressed as a linear combination of the functions in the basis  $\boldsymbol{\psi}^{\mathbf{u},1/2}$ .

*The new enrichment is distinct from the Lecampion enrichment [36] for  $\lambda \neq 1/2$ .*

The enrichment functions (30) and (31) do not assume any particular boundary conditions at the faces of the crack. For a particular case when the shear traction at the faces of a fluid-driven crack does not have a singular component, and the normal traction on both sides of the crack is equal to the singular pressure,

$$\sigma_{\theta\theta}(\pi) = \sigma_{\theta\theta}(-\pi) = -p, \quad \sigma_{r\theta}(\pi) = \sigma_{r\theta}(-\pi) = 0, \quad (32)$$

the four constants involved in (29) must satisfy

$$C_1 = C_3 = 0, \quad C_4 = C_2 \frac{1 + \lambda}{1 - \lambda} \quad (33)$$

and the general singular solution yields the following crack width and pressure:

$$w = A r^\lambda, \quad p = \frac{E'}{4} A \lambda \cot(\pi\lambda) r^{\lambda-1} \quad (34)$$

where  $A = C_2 \frac{8}{E'} \frac{1+\lambda}{1-\lambda} \sin(\lambda\pi)$ . Note that (34) agrees with the asymptotic behavior obtained by local analysis [47]. For  $\lambda \neq \frac{1}{2}$ , the singular pressure in (34) is non-zero.

For the general power-law crack tip asymptote with the exponent  $\lambda$ , Lecampion [36] used the displacement enrichment basis different from (30). The basis used in [36] included the following functions:

$$\boldsymbol{\Psi}^{\mathbf{u},\lambda} = r^\lambda \{ \sin(\lambda\theta), \cos(\lambda\theta), \sin(\lambda\theta) \sin\theta, \cos(\lambda\theta) \sin\theta \} \quad (35)$$

which reduce to the basis  $\boldsymbol{\psi}^{\mathbf{u}}$  in (24) for  $\lambda = 1/2$ . However, for  $\lambda \neq 1/2$ , the basis  $\boldsymbol{\Psi}^{\mathbf{u},\lambda}$  in (35) and the basis  $\boldsymbol{\psi}^{\mathbf{u},\lambda}$  in (30) span different function spaces, because the functions  $g_1(\theta, \lambda) = \sin(\lambda\theta) \sin\theta$  and  $g_2(\theta, \lambda) = \cos(\lambda\theta) \sin\theta$ ,

involved in the angular part of  $\Psi^{u,\lambda}$ , cannot be expressed as linear combinations of the four angular functions in  $\psi^{u,\lambda}$ . To show this, we denote the angular functions in  $\psi^{u,\lambda}$  as  $f_1(\theta, \lambda) = \sin(\lambda\theta)$ ,  $f_2(\theta, \lambda) = \cos(\lambda\theta)$ ,  $f_3(\theta, \lambda) = \sin((\lambda - 2)\theta)$  and  $f_4(\theta, \lambda) = \cos((\lambda - 2)\theta)$ , and construct the Wronskian for the six functions  $g_1, g_2$  and  $f_i$  ( $i = 1, \dots, 4$ ):

$$W(\theta; \lambda) = \det \begin{bmatrix} g_1 & g_2 & f_1 & \cdots & f_4 \\ \frac{\partial g_1}{\partial \theta} & \frac{\partial g_2}{\partial \theta} & \frac{\partial f_1}{\partial \theta} & \cdots & \frac{\partial f_4}{\partial \theta} \\ \vdots & \vdots & \vdots & \ddots & \vdots \\ \frac{\partial^5 g_1}{\partial \theta^5} & \frac{\partial^5 g_2}{\partial \theta^5} & \frac{\partial^5 f_1}{\partial \theta^5} & \cdots & \frac{\partial^5 f_4}{\partial \theta^5} \end{bmatrix} \quad (36)$$

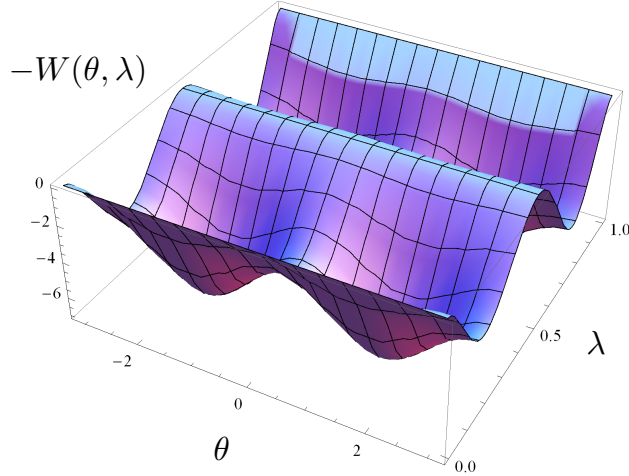


Figure 5: Negative of the Wronskian,  $-W(\theta; \lambda)$ , for  $-\pi \leq \theta \leq \pi$  and for  $0 \leq \lambda \leq 1$

Fig. 5 shows the plot of the negative of the Wronskian,  $-W(\theta; \lambda)$ , for  $-\pi \leq \theta \leq \pi$  and for  $0 \leq \lambda \leq 1$ . It is seen that for  $\lambda \neq 0, 1/2, 1$ , the Wronskian is a nonzero function of  $\theta$ , so that the six functions  $g_1, g_2$  and  $f_i$  ( $i = 1, \dots, 4$ ) are linearly independent for these values of  $\lambda$ . The consequence is that  $\text{span } \Psi^{u,\lambda}$  is not sufficient to represent the elastic solution in the vicinity of the crack tip, which corresponds to the asymptotic crack width (20), for  $\lambda \neq 0, 1/2, 1$ . Section 6.2 presents a numerical convergence study, with  $\lambda = 2/3$ , which demonstrates that using the enrichment functions  $\psi^{u,\lambda}$ , the  $O(h^2)$  optimal convergence rate is recovered using the XFEM. In addition, our numerical experiments show that the enrichment functions  $\Psi^{u,\lambda}$  do not achieve this convergence rate.

### *Other power law enrichments*

Huang et al. [60] modeled a crack in a thin film on a substrate using another set of four singular enrichment functions that involve a power law dependence  $r^\lambda$  on the distance  $r$  to the crack tip, for  $0 < \lambda < 1$ . That enrichment was based on the asymptotic solution for the crack tip at a bi-material interface, in which the exponent  $\lambda$  is determined as a function of the Dundurs parameters [61]. The enrichment in [60] and the present power law enrichment (30) are not equivalent, and they span solutions to different elastic problems. In the range  $0 < \lambda < 1$ , these two enrichments are equivalent only for  $\lambda = \frac{1}{2}$ , corresponding to a crack in a homogeneous material under the assumptions of LEFM.

### *5.3. Linear dependence of the power-law tip enrichment*

As it is mentioned above, the singular tip enrichment functions  $\boldsymbol{\psi}^{\mathbf{u},\lambda}$  are multiplied by the Lagrange functions  $N_i$  in the approximation (23), in order to achieve partition of unity. The blending strategy in (23), adopted after Fries [38] for its simplicity in comparison to other available techniques [48], restores the partition of unity in the blending elements. In this approach, the singular shape functions  $N_i(\mathbf{x})\boldsymbol{\psi}_j^{\mathbf{u},\lambda}(\mathbf{x})$  are introduced in all four nodes of tip-enriched elements.

While the classical square-root tip enrichment (24) is represented by four linearly-independent functions  $\boldsymbol{\psi}_j^{\mathbf{u}}(\mathbf{x})$ , Fries [38] shows that the singular shape functions  $N_i(\mathbf{x})\boldsymbol{\psi}_j^{\mathbf{u}}(\mathbf{x})$ , involved in the approximation (23) of the displacement in a bi-linear element, are linearly dependent if all nodes of the element are enriched with the square-root tip enrichment (24). In particular, among these 16 functions (4 nodes of a quadrilateral element  $\times$  4 enrichment functions (24)), only 14 are linearly-independent. This linear dependency does not manifest itself in the global stiffness matrix if there are tip-enriched elements in which some of the nodes are not tip-enriched. However, in an XFEM formulation where the tip enrichment is introduced in all nodes in the set  $I_t^*$  and a ramp function  $R_t$  is used to blend the tip enrichment, i.e. if in the tip-enriched elements all four nodes are tip-enriched (which is the case for the present *XFEM-t* formulation, see (23)), this linear dependence results in the rank deficiency of the global stiffness matrix of 2, per displacement component, per crack tip. For the case  $\lambda = 1/2$  Fries [38] demonstrated that it is possible to obtain a modified global stiffness matrix with full rank by eliminating from the system of equations those shape functions that can be expressed as linear combinations of the other shape functions.

Similarly, the general linearly-independent power-law tip enrichment bases for the displacement (30) and stress (31) result in linearly dependent shape functions  $N_i(\mathbf{x})\psi_j^{\mathbf{u},\lambda}(\mathbf{x})$  and  $N_i(\mathbf{x})\psi_j^{\sigma,\lambda}(\mathbf{x})$  in a bi-linear quadrilateral element with four tip-enriched nodes. Among the 16 functions for the displacement  $N_i(\mathbf{x})\psi_j^{\mathbf{u},\lambda}(\mathbf{x})$ , only 14 are linearly-independent, and the same applies to the 16 functions for the stress  $N_i(\mathbf{x})\psi_j^{\sigma,\lambda}(\mathbf{x})$ . In addition, in the present *XFEM-t* approximation the stress shape functions (section 4.2) are defined on the element level and are discontinuous at the FE nodes and edges, which multiplies the rank of the linear deficiency from the stress shape functions by the number  $n_{tip}$  of the elements in the set  $\mathcal{B}$  (elements with stress degrees of freedom). This results in a rank deficiency of the global stiffness matrix of  $4 + 6n_{tip}$  per crack tip, on account of the 2 displacement components and 3 components of the symmetric stress tensor.

In order to obtain a stiffness matrix with full rank, we choose to eliminate from the displacement representation (23) two displacement functions  $N_i(\mathbf{x})\psi_j^{\mathbf{u},\lambda}(\mathbf{x})$  for  $j = 3, 4$  and any node  $i \in I_t$ , and to eliminate from the stress representation, given in section 4.2, two stress functions  $N_i(\mathbf{x})\psi_j^{\sigma,\lambda}(\mathbf{x})$  for  $j = 3, 4$  and any node  $i \in I_e$  for each element  $e \in \mathcal{B}$ . Using a similar procedure to that used by Fries [38], in Appendix B we show that the rank deficiency can be removed by expressing these two displacement functions in terms of the remaining fourteen of the sixteen functions  $N_i(\mathbf{x})\psi_j^{\mathbf{u},\lambda}(\mathbf{x})$  for an element aligned with the Cartesian axes. Moreover, the same applies to the stress functions  $N_i(\mathbf{x})\psi_j^{\sigma,\lambda}(\mathbf{x})$ .

In the numerical results presented in this paper, all stiffness matrices had full rank by virtue of this elimination of the unnecessary shape functions.

Fries's corrected XFEM has been used for a three-dimensional problem in [62], where the linear dependency in the shape functions was removed by eliminating several (one or three) functions from the basis (24). This approach removes more shape functions than required to achieve the full rank. In contrast, only linearly-dependent shape functions are removed in the present approach.

## 6. Numerical results

In this section we present a comparison of the  $P \rightarrow W$  and  $P\&W$  schemes with the power law tip enrichment (*XFEM-t*) and without the tip enrichment (*XFEM-s*), for a problem in which the singularity in the crack-tip fields corresponds to one of the two limiting regimes of HF propagation:  $\lambda =$

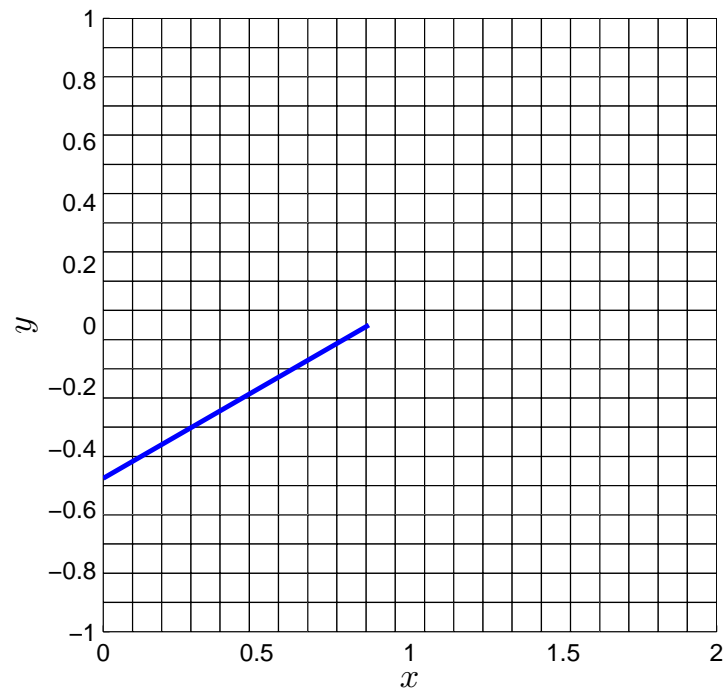
1/2 (toughness-dominated) or  $\lambda = 2/3$  (viscosity-dominated). We consider a model problem for which a closed-form solution is available, namely the asymptotic crack-tip solution obtained for  $1/2 \leq \lambda < 1$  in Section 5.1, with the constants given by (33) and  $C_2 = 1$ .

We consider a square domain  $V = [0, 2] \times [-1, 1]$  discretized into a mesh of  $N \times N$  square elements of side length  $h = 2/N$ . The crack is assumed to have a unit length  $\ell = 1$  and is inclined at  $30^\circ$  to the  $x$ -axis (Fig. 6). The crack's open end is placed at  $\mathbf{x}_o = (0, -0.5)$ . A Dirichlet boundary condition (7) is prescribed along the outer boundary  $\Gamma$  by setting the displacements at the nodes along this boundary to the displacements associated with the asymptotic solution given in Section 5.1. In addition, in the sign-enriched element adjacent to  $\Gamma$ , which encapsulates the crack's left end, the values of four sign-enrichment degrees of freedom, associated with the two nodes along  $\Gamma$  and two displacement components, are set so that the displacement at the crack's open end  $\mathbf{x}_o = (0, -0.5)$ , on each crack face, is given by the asymptotic solution. The applied shear traction along the crack faces is zero,  $\hat{\sigma}_s = 0$ . The boundary values for the crack width and the pressure, given by (34), are used in both the  $P \rightarrow W$  and the  $P\&W$  schemes to set the boundary conditions according to (1) and (2), respectively. In all simulations, the Poisson's ratio was set to  $\nu = 0.2$ . The radius of the displacement tip enrichment in  $XFEM-t$  simulations was  $\rho = 0.25$ . The continuity of the displacement approximation at the virtual crack tip in  $XFEM-s$  simulations was restored by using the ramp function  $R_s(\mathbf{x})$  (see Section 4.1).

### 6.1. Comparison of $P \rightarrow W$ and $P\&W$

We first compare the performance of the  $P \rightarrow W$  and  $P\&W$  formulations using the  $XFEM-t$  and  $XFEM-s$  enrichment strategies with the same finite element mesh. Fig. 7 shows the relative errors in the crack width obtained using  $N = 41$  and  $N = 321$  elements along the side of the domain  $V$ , for the case  $\lambda = 2/3$ . The crack's open end corresponds to  $s = 0$ , and the crack tip corresponds to  $s = 1$ . In the  $P\&W$  formulation, two elements were included in the tip zone  $\Sigma_t$  (i.e.  $n_{tip} = 2$ ). The resulting boundary between the channel  $\Sigma_c$  and the tip  $\Sigma_t$  is depicted in the figure by the vertical solid black line. For the  $XFEM-s$  schemes, the results are not shown for the finite element that includes the crack tip, since in this last element, the crack is virtually extended to the element edge, and the displacement jump is only approximated in an average sense (see section 4). For the case  $N = 321$ , only

Figure 6: Crack configuration and the FEM mesh for  $N = 21$ .



20% of the crack in the vicinity of the crack tip,  $s \in (0.8, 1)$ , is shown in the figure in order to emphasize the difference of the results near the crack tip.

We can see that among the four schemes presented, the combination  $P\&W / XFEM-t$  is the best. Comparing the two tip-enriched schemes  $P\&W / XFEM-t$  and  $P \rightarrow W / XFEM-t$ , we see that the  $P\&W$  scheme provides a more accurate solution near the crack tip. The solution of the  $P\&W / XFEM-t$  scheme near the crack tip is approximately one order more accurate at the channel-tip boundary than that of  $P \rightarrow W / XFEM-t$  scheme. Further away from the crack tip, the results from these two schemes coincide, and as  $N$  is increased while  $n_{tip} = 2$  is kept constant, the region of equivalence of these two solutions is extended to cover most of the crack. This behavior is to be expected, since when the tip zone  $\Sigma_t$ , over which the width boundary condition (2) is specified, vanishes, the  $P\&W$  formulation reduces to the  $P \rightarrow W$  formulation. However, in practice it may only be feasible to use a moderate number of elements to cover the crack (e.g in a fully-coupled problem for a propagating HF), while the accuracy of the solution near the crack tip has a dominant effect on the accuracy of the total evolution of the solution for a propagating HF. For such cases, the  $P\&W / XFEM-t$  formulation is superior to  $P \rightarrow W / XFEM-t$ .

There is another, even more important, reason why the  $P \rightarrow W$  formulation is not suitable for use in a fully-coupled problem for a propagating HF. In a coupled model, if the  $P \rightarrow W$  takes the pressure as input data and solves for the crack width, this pressure has to be obtained from the solution of the nonlinear lubrication equation that governs the fluid flow (see e.g. [2]). The solution to this nonlinear equation for the pressure has to be obtained iteratively. Given the fact that the pressure is singular at the crack tip when the fluid and the fracture fronts coalesce [39], an iterative solution for the pressure is likely to be inaccurate at the nodes very close to the crack tip. This inaccurate numerical pressure cannot be replaced by an available asymptotic solution, due to the vanishingly small validity region of such a solution for the pressure. On the other hand, the  $P\&W$  formulation does not have this disadvantage because it separates the tip zone  $\Sigma_t$ , in which the pressure is singular, from the channel zone  $\Sigma_c$  where the pressure is finite, and only requires the input data for the XFEM for the pressure in the channel. An iterative solution of the nonlinear lubrication equation for the pressure in the channel only (as required for the  $P\&W$  formulation) is less prone to instability than the solution for the pressure in the complete crack including the tip (as required for the  $P \rightarrow W$  formulation).

The difference between  $P \rightarrow W$  and  $P\&W$  is more significant for the case of the  $XFEM-s$  enrichment and the fine mesh with  $N = 321$ . It may seem surprising that the accuracy of the  $P \rightarrow W$  solution is not increased when  $N$  is increased from  $N = 41$  to  $N = 321$ . The reason for this is that this scheme, as well as the  $P\&W / XFEM-s$  scheme, is sensitive to the type of the cut in the tip element, due to the fact that the actual crack tip is approximated only in a weak sense and that the boundary conditions along the crack extension  $\bar{\Sigma}$  beyond the actual crack tip are not satisfied by the weak form (see Section 4). Oscillation of the approximation errors for the  $XFEM-s$  schemes is further discussed in Section 6.2. The  $P\&W$  scheme provides a higher accuracy of the crack width near the channel-tip boundary, i.e. at the nodes which are used to predict fracture propagation in a coupled model. Note that the  $P \rightarrow W / XFEM-s$  cannot achieve the accuracy level of 10% near the crack tip, while the  $P\&W$  scheme achieves the accuracy level of 3% in this example. To improve on the quality of the  $P \rightarrow W / XFEM-s$  solution, a modified scheme with correct boundary conditions along the crack extension  $\bar{\Sigma}$  could be used, as discussed in Section 4. However, the general disadvantage of the  $P \rightarrow W$  scheme regardless of the employed enrichment strategy outlined above for a fully-coupled HF problem (vs.  $P\&W$ ) does not warrant the use of such modifications. On the other hand, the results of the  $P\&W / XFEM-s$  have acceptable accuracy. Another observation from these plots that can be useful in the design of XFEM algorithms is that, in order to predict fracture propagation within a coupled  $P\&W$  scheme with the present structure of the sign enrichment in the tip element, it may be advantageous to use the crack width at a node a few elements away from the channel-tip boundary, rather than the node on the channel-tip boundary.

While the two tip-enriched schemes offer higher accuracy by including the special singular enrichment derived above, the sign-enriched  $P\&W / XFEM-s$  scheme can offer a more efficient solution with an acceptable accuracy, when it is used to model propagation of a hydraulic fracture with the full coupling between the elasticity and the fluid flow [2]. The efficiency of the  $P\&W / XFEM-s$  in comparison to the  $XFEM-t$  schemes in solving a dynamic problem is due to the following (i) when the crack propagates within one finite element, there is no need to update the stiffness matrix; (ii) upon crack propagation, the enrichment has to be updated only for those elements that are cut by the crack for the first time; (iii) no singular integrals have to be calculated to obtain the stiffness matrix; and (iv) the size of the stiffness matrix, that has to be inverted multiple times at each crack propagation step, is reduced

(see [2] for more details). The combination  $P \rightarrow W / XFEM-s$  cannot offer such accuracy-efficiency trade-off because its results are prone to inaccuracy near the crack tip, and because of the general disadvantage of the  $P \rightarrow W$  approach for a fully-coupled HF problem with singular crack-tip pressure, as discussed above.

### 6.2. Convergence study

Next we study the convergence rates of the XFEM schemes as the mesh size  $h$  is reduced. Odd numbers of elements along the side of the square domain  $V$  were varied between  $N = 21$  and  $N = 321$ . More meshes were considered for the  $XFEM-s$  schemes in an attempt to reduce the sensitivity of the numerically obtained convergence rates to the way in which the crack cuts the tip element (the cut type). In the  $P\&W$  formulation, two elements were included in the tip zone  $\Sigma_t$  (i.e.  $n_{tip} = 2$ ) for all  $N$ . The approximation error in the displacement field was quantified by means of the integral  $L_2$ - and  $H_1$ -norms as follows:

$$E_{u,L_2} = \frac{\|\mathbf{u} - \mathbf{u}^{ref}\|_{L_2(V)}}{\|\mathbf{u}^{ref}\|_{L_2(V)}}, \quad E_{u,H_1} = \frac{\|\mathbf{u} - \mathbf{u}^{ref}\|_{H_1(V)}}{\|\mathbf{u}^{ref}\|_{H_1(V)}}$$

where the superscript *ref* denotes the reference solution, and

$$\|\mathbf{u}\|_{L_2(V)} = \sqrt{\int_{V \setminus \Sigma} (u_1)^2 + (u_2)^2 dV}$$

$$\|\mathbf{u}\|_{H_1(V)} = \sqrt{\|\mathbf{u}\|_{L_2(V)}^2 + \int_{V \setminus \Sigma} \sum_{i=1,2} \sum_{j=1,2} (u_{i,j})^2 dV}$$

The error in the crack width was quantified by means of the  $L_2$ -norm over the complete crack  $\Sigma$ ,

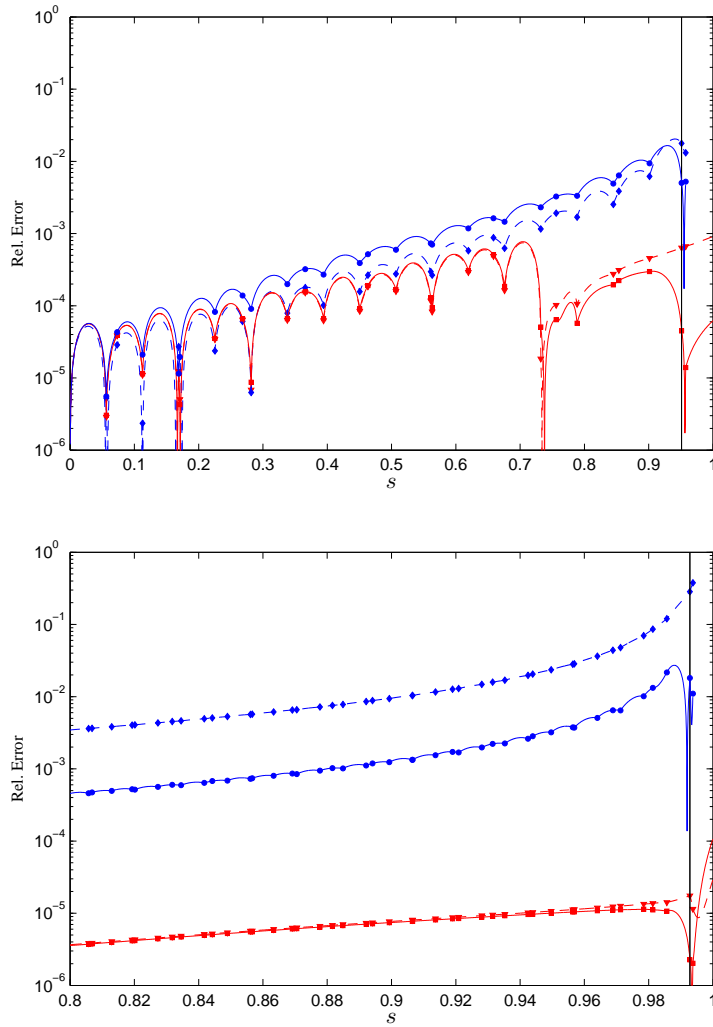
$$E_w = \frac{\|w - w^{ref}\|_{L_2(\Sigma)}}{\|w^{ref}\|_{L_2(\Sigma)}} \quad (37)$$

where

$$\|w\|_{L_2(\Sigma)} = \sqrt{\int_{\Sigma} w^2 ds}$$

Figure 8 shows the convergence rates of the errors for the  $P \rightarrow W / XFEM-t$  and  $P \rightarrow W / XFEM-s$  schemes for  $\lambda = 2/3$ . Figure 9 shows

Figure 7: Relative error  $|w - w^{ref}|/w^{ref}$  in the crack width for  $\lambda = 2/3$ , obtained with  $N = 41$  (top: the complete crack) and  $N = 321$  (bottom: to emphasize the results only 20% of the crack in the vicinity of the tip,  $s \in (0.8, 1)$  is shown). The crack tip is at  $s = 1$ . Results correspond to:  $P \rightarrow W$  (dashed red with triangles for  $XFEM-t$ , dashed blue with diamonds for  $XFEM-s$ ) and  $P\&W$  (solid red with squares for  $XFEM-t$ , solid blue with circles for  $XFEM-s$ ). The vertical solid black line in each plot depicts the location of the boundary between the channel  $\Sigma_c$  and the tip  $\Sigma_t$  for the  $P\&W$  formulation.



the convergence rates of the errors for the  $P\&W / XFEM-t$  scheme for  $\lambda = 1/2, 2/3$  and the  $P\&W / XFEM-s$  scheme for  $\lambda = 2/3$ . These results reveal that the tip-enriched schemes  $P \rightarrow W / XFEM-t$  and  $P\&W / XFEM-t$  with the new tip enrichment for the displacement and the stress (for  $P\&W$ ) achieve optimal convergence orders corresponding to the bi-linear elements in the underlying FEM mesh,

$$\|w - w^{ref}\|_{L_2(\Sigma)} \sim O(h^2) \quad (38)$$

$$\|\mathbf{u} - \mathbf{u}^{ref}\|_{L_2(V)} \sim O(h^2), \quad \|\mathbf{u} - \mathbf{u}^{ref}\|_{H_1(V)} \sim O(h) \quad (39)$$

This confirms the validity of the new enrichment for the displacement and the stress for a general power law index  $1/2 \leq \lambda < 1$ . In contrast, our numerical experiments show that the enrichment functions (35) presented in [36] do not achieve these optimal convergence rates.

The convergence rates in the  $XFEM-s$  solutions show less uniformity between  $P \rightarrow W$  and  $P\&W$  schemes. The integral norms of the errors for the  $P\&W / XFEM-s$  scheme have higher convergence rates, and the results for the  $P\&W / XFEM-s$  have smaller (or equivalent) overall errors in the crack width  $E_w$  and in the displacement  $E_{u,L_2}$  for all values of  $h$  used in this example, as shown in Fig. 10. In particular, it is seen that for  $N = 41$  the errors for the two  $XFEM-s$  solutions are almost identical, but for  $N = 321$  the  $P\&W / XFEM-s$  is more accurate, which agrees with the detailed plots of the crack width shown in Fig. 7 for these two values of  $N$ .

In comparison with the  $XFEM-t$  schemes, the results from  $XFEM-s$  show significant oscillations due to the representation of the crack tip by the sign enrichment alone, the imposition of the crack width field in a weak sense and the discrepancy between the continuity in the displacements beyond the actual crack tip and the boundary conditions imposed along the crack extension  $\bar{\Sigma}$ ; the accuracy of such a representation depends on how the crack cuts the tip-enclosing finite element, i.e. the cut type in the tip element. It is observed that the results for  $P\&W / XFEM-s$  are less sensitive to the cut type as they exhibit smaller oscillations.

It should be noted that the stress enrichment, required in the  $P\&W / XFEM-s$ , employs the same shape functions as those used for the displacement (see Section 4) rather than requiring a special set of shape functions conforming to the derivatives of the displacement shape functions as in  $P\&W$

/ *XFEM-t*. Convergence rates for the same enrichment strategy (displacement and stress are approximated by the bi-linear Lagrange functions and sign enrichment) were studied for the mixed-hybrid XFEM in [40] for the problem of a prescribed displacement jump along the interface between an inhomogeneity and the enclosing medium. They reported linear convergence of the error in the interfacial displacement and the convergence rate of 1.5 in the  $L_2$ -norm of the displacement in the domain, attributing the reduced convergence rate in the interfacial displacement to shear-locking for that problem [40]. In the present problem, which is, in fact, more difficult for the XFEM to solve due to the presence of the singular fields associated with the crack, the convergence rate of *P&W / XFEM-s* for the displacement in the domain is equivalent to that obtained in [40] and the convergence rate for the crack width is slightly above the rate obtained in [40] for the interfacial displacement (see Fig. 9).

As discussed above, the quality of the *XFEM-s* solutions can be improved by using correct boundary conditions along the crack extension  $\bar{\Sigma}$  within the weak form. The low convergence rates for  $P \rightarrow W / XFEM-s$  can be a consequence of such inequivalence of the boundary conditions.

In our previous work [2] we investigated the convergence of the coupled model for HF propagation, which used *P&W / XFEM-s* with no ramp function in the tip element, while all four nodes of the tip element were enriched with the sign enrichment, thus violating the continuity requirement across  $\partial V_*$ . For such formulation, linear convergence in the crack width was observed for the present numerical example,

$$\|w - w^{ref}\|_{L_2(\Sigma)} \sim O(h) \quad (40)$$

### 6.3. *P&W with a fixed tip zone*

In the convergence study in the previous section, exactly two elements were included in the tip zone  $\Sigma_t$  in the *P&W* formulation ( $n_{tip} = 2$ ). As was mentioned in Section 6.1, when  $N$  is increased, the size of the tip zone is decreased and eventually the *P&W* formulation converges to  $P \rightarrow W$ . To assess the convergence of the pure *P&W / XFEM-t* formulation in which the size of the tip zone  $\Sigma_t$  is fixed and does not decrease with  $N$ , we perform simulations in which the tip zone  $\Sigma_t = \{s : s \in (0.9, 1)\}$  covers the 10% of the crack closest to the tip, for all  $N$ .

In the simulations, we observed a reduced accuracy of the results when both types of the boundary conditions (2) are present in one finite element,

Figure 8: Convergence rates of the errors in the crack width and the displacement field, for the  $P \rightarrow W$  formulations and  $\lambda = 2/3$ . Results correspond to:  $XFEM-t$  (solid red with squares) and  $XFEM-s$  (solid blue with circles).

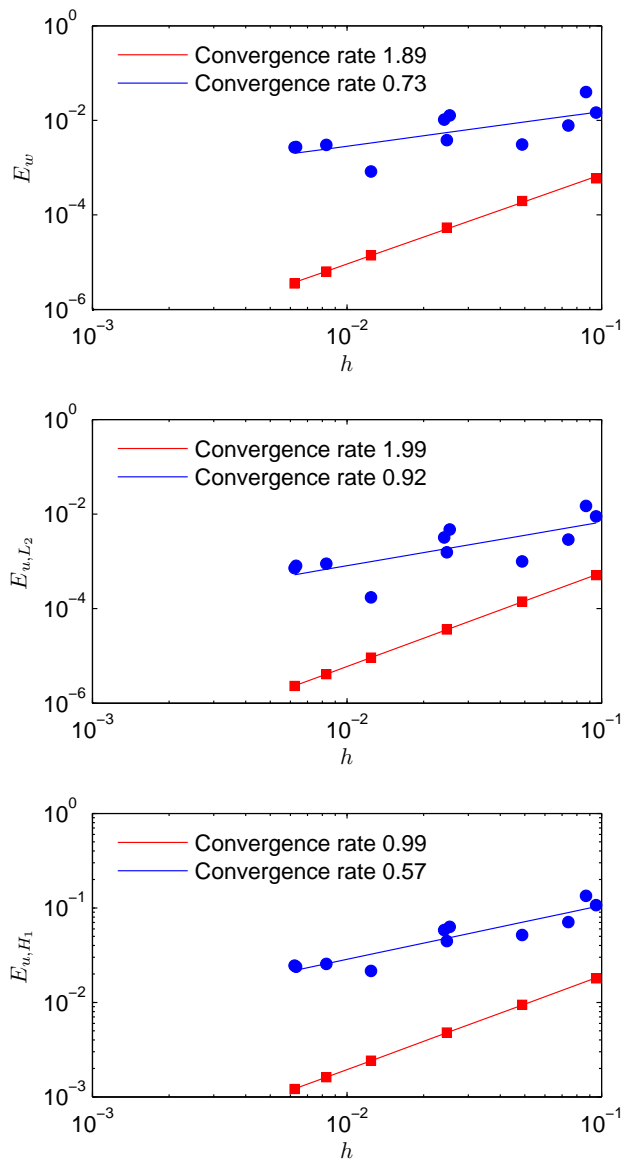


Figure 9: Convergence rates of the errors in the crack width and the displacement field for the  $P&W$  formulations. Results correspond to:  $XFEM-t$  and  $\lambda = 2/3$  (solid red with squares),  $XFEM-t$  and  $\lambda = 1/2$  (dashed red with triangles), and  $XFEM-s$  and  $\lambda = 2/3$  (solid blue with circles).

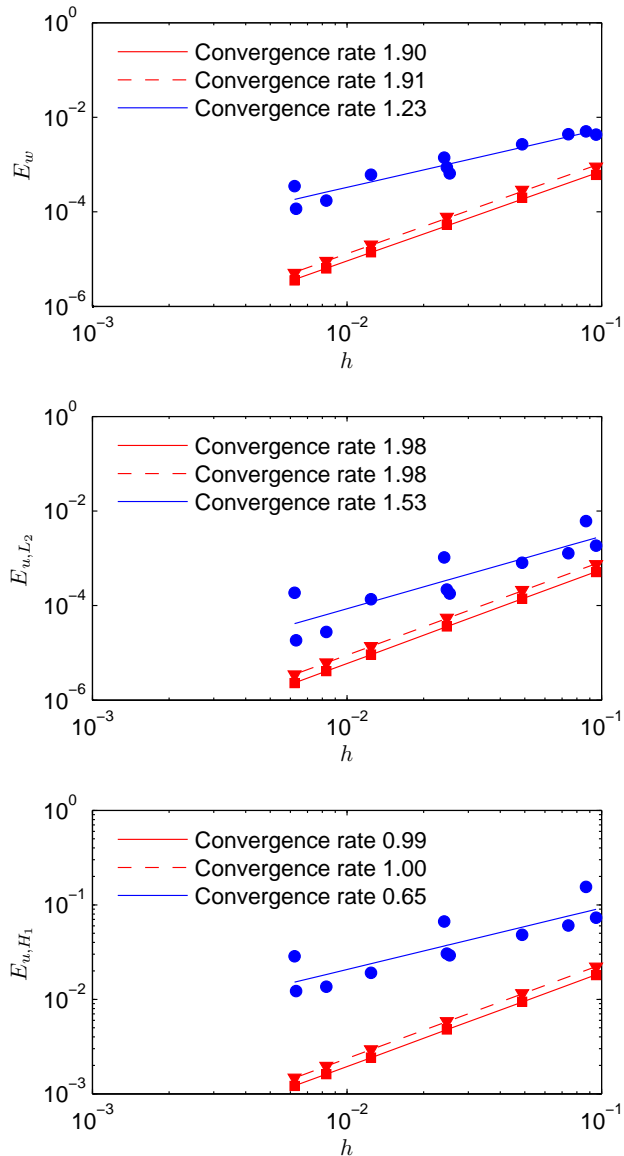
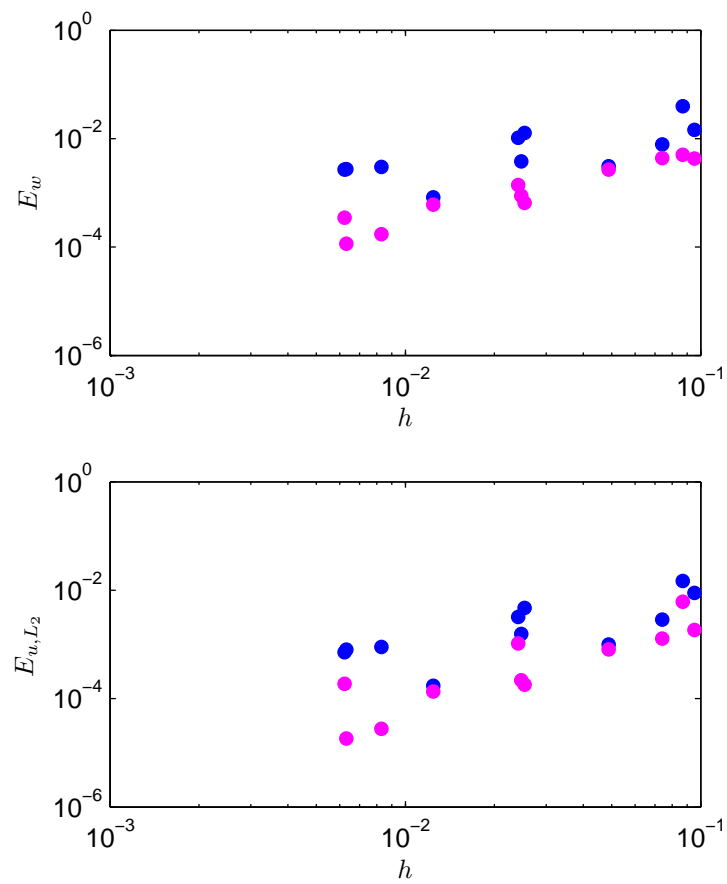


Figure 10: Comparison of the convergence rates of the errors in the crack width and the displacement field, for  $P \rightarrow W / XFEM-s$  (blue) and  $P\&W / XFEM-s$  (magenta). Results correspond to  $\lambda = 2/3$ .

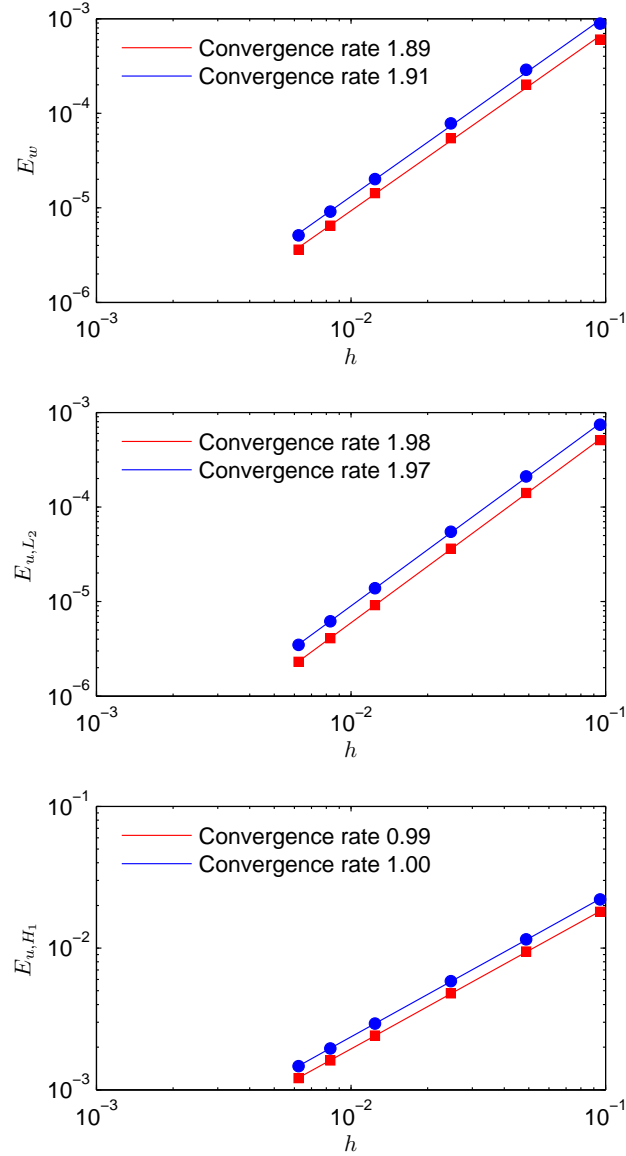


i.e. when in a single finite element one has to compute integrals over  $\Sigma_c$  and  $\Sigma_t$  in (15) - (18). Thus we choose to use only one of the two conditions from (2) in every single finite element cut by the crack. To achieve this, we increase or decrease the length of  $\Sigma_t$  within one finite element that encloses the point  $s = 0.9$ , to the closest edge of that element. As the result, for all  $N$ , the length of  $\Sigma_t$  is approximately 10%, and no single finite element has both types of boundary conditions (2) present simultaneously. The results of this version of the  $P\&W / XFEM-t$  formulation for  $\lambda = 1/2, 2/3$  are shown in Fig. 11. Optimal convergence rates for all three computed errors are obtained. This once again confirms the validity of the new enrichment for the displacement and the stress for a general power law index  $1/2 \leq \lambda < 1$ .

## 7. Conclusions

In this paper we have explored the accuracy and convergence properties of a number of schemes and enrichment strategies useful for modeling propagating HF using the XFEM [1, 2]. The primary role of the XFEM in a fully coupled HF propagation model is to repeatedly solve a boundary value problem to determine the deformation response of the solid medium to the fluid pressures applied to the crack faces. By introducing specialized enrichment functions around the crack, the XFEM is able to avoid the re-meshing process required of the FEM when adapting to the moving boundaries of propagating cracks. If there is a fluid lag, so the fluid and fracture fronts are separate, then the pressure field is finite at the crack tip and the so-called  $P \rightarrow W$  XFEM scheme can be used to determine the standard Neumann to Dirichlet map. However, if the fluid and fracture fronts coalesce then the pressure field is singular at the crack tip, which renders the  $P \rightarrow W$  XFEM scheme a poor choice since capturing this singular behavior numerically is inaccurate and using an asymptotic solution for the pressure in the tip is precluded since its region of validity becomes vanishingly small. In this case, the preferred formulation is to make use of the appropriate asymptotic expansion for the *finite* crack width in the vicinity of the tip and prescribe the *finite* pressure in the so-called channel region away from the tip. This mixed boundary value formulation, which we have named the  $P\&W$  scheme, enables the XFEM to model propagating HF with coalescent fluid and fracture fronts and a singular pressure field. In this paper we have also presented a new  $P\&W$  variational formulation, which is a modification of the mixed hybrid XFEM by [40].

Figure 11: Convergence rates of the errors in the crack width and the displacement field, for the  $P\&W / XFEM-t$  scheme with  $\Sigma_t$  covering the 10% of the crack closest to the tip. Results correspond to:  $\lambda = 2/3$  (solid red with squares) and  $\lambda = 1/2$  (solid blue with circles).



Propagating hydraulic fractures typically involve multiple physical processes that can switch dominance as the fracture evolves. In order to be able to capture these different physical processes when their characteristic length scale is of the same order as the computational length scale, it is necessary to be able to represent crack width fields whose asymptotic behaviors span the range of power laws  $\frac{1}{2} \leq \lambda < 1$ . This class of power laws needs to be implemented in the prescribed width fields within the crack for example in the *P&W* scheme as well as in the crack tip enrichment functions. Numerical experiments show that existing tip enrichment functions available in the literature [36] for such power laws do not achieve optimal convergence. We have therefore derived a new set of enrichment functions for the displacement and the stress fields that span the required range of power laws. We have presented numerical results that demonstrate that when using these new tip enrichment functions, the XFEM scheme is able to recover the optimal  $O(h^2)$  convergence rate we expect of the underlying piece-wise linear FEM discretization. If tip enrichment is applied to all the nodes of tip enriched elements, then the resulting stiffness matrix is singular due to the linear dependence of some of the enrichment shape functions. For this new class of enrichment functions, we have shown how to eliminate this linear dependence by expressing the shape functions associated with the stiffness matrix null space in terms of the remaining linearly independent shape functions. The resulting stiffness matrix has full rank. The numerical results in this paper are presented for two values of power law index  $\lambda$ . This is appropriate for a wide class of one dimensional HF propagating in a state of plane strain [35] in which the power law index does not change during the evolution of the fracture. However, for planar HF in a 3D elastic medium one may need to change the power law exponent  $\lambda$ , as the propagation regime changes along the fracture boundary [35, 27]. To choose a suitable power law  $\lambda$  for enrichment in this case, one may use an effective power law applicable over multiple length scales or a tangent power law whose index corresponds to the dominant length scale applicable at that part of the fracture boundary at that particular time.

While the XFEM, with the appropriate tip enrichment, is able to achieve optimal accuracy without re-meshing, the computational burden of integrating singular enrichment functions for each new trial position of the fracture front is not insignificant. We have thus sought, sub-optimal, but more efficient schemes that can also be used to model propagating HF with reasonable precision. One such scheme [2] is the so-called *XFEM-s* scheme in

which only discontinuous enrichment functions are introduced to represent the crack and there is no tip enrichment. However, the pressure field (in the  $P \rightarrow W$  scheme) and the tip width field (in the  $P\&W$  scheme) are imposed in a weak sense. To distinguish it from the  $XFEM-s$  scheme, the XFEM scheme with full tip enrichment is named the  $XFEM-t$  scheme. In order to provide a practical guide for the development of XFEM algorithms for modeling propagating HF, we have conducted a detailed study of the accuracy and convergence characteristics of the following schemes :  $P \rightarrow W / XFEM-t$ ,  $P\&W / XFEM-t$ ,  $P \rightarrow W / XFEM-s$ , and  $P\&W / XFEM-s$ . To assess the performance of these schemes we have considered a static crack subjected to precisely the same type of boundary conditions that would be imposed at any given time-step in the XFEM component of a fully coupled algorithm when modeling a propagating crack. The findings are summarized below:

(i) *Spatial error distribution*: From a detailed spatial plot of the error in the width field it follows that the  $P\&W / XFEM-t$  scheme is uniformly the most accurate scheme. Away from the tip both  $XFEM-t$  schemes have almost identical accuracy profiles, while the  $P\&W / XFEM-t$  scheme is approximately one order of magnitude more accurate than the  $P \rightarrow W / XFEM-t$  scheme close to the channel-tip boundary. The  $XFEM-t$  schemes outperform the  $XFEM-s$  schemes. The  $P\&W / XFEM-s$  scheme has more accurate results than the  $P \rightarrow W / XFEM-s$  scheme.

(ii) *Global error measures - convergence*: By refining the underlying FEM mesh the following convergence rates were established:

$$\begin{aligned}
& E_{w,L_2}^{XFEM-t} = O(h^2), \quad E_{u,L_2}^{XFEM-t} = O(h^2), \quad \text{and} \quad E_{u,H_1}^{XFEM-t} = O(h), \\
& E_w^{P \rightarrow W / XFEM-s} = O(h^{0.7}), \quad E_{u,L_2}^{P \rightarrow W / XFEM-s} = O(h), \quad \text{and} \quad E_{u,H_1}^{P \rightarrow W / XFEM-s} = \\
& O(h^{3/5}), \\
& E_w^{P\&W / XFEM-s} = O(h^{1.2}), \quad E_{u,L_2}^{P\&W / XFEM-s} = O(h^{1.5}), \quad \text{and} \quad E_{u,H_1}^{P\&W / XFEM-s} = \\
& O(h^{3/5})
\end{aligned}$$

The quality of the  $XFEM-s$  solutions can possibly be further improved by avoiding the violation of the boundary conditions along the crack extension beyond the crack tip to the farthest edge of the encompassing finite element.

Thus in this paper we have derived a new set of enrichment functions that are required by the XFEM to model the multiscale processes typically encountered for propagating HF. We have also shown how to restore the stiffness matrix associated with these enrichment functions to full rank. The convergence tests establish the optimal convergence of the  $XFEM-t$  schemes and the sub-optimal but linear/super-linear convergence of the  $XFEM-s$  schemes

for both  $P \rightarrow W$  and  $P\&W$  classes of boundary value problem. These results should prove very useful in the design of new XFEM algorithms to model propagating HF in complex media.

## Acknowledgments

The MATLAB codes used for numerical simulations in this paper were based on the original MATLAB software package for XFEM implementation in a domain with a crack by Dr.-Ing. T.-P. Fries (RWTH Aachen University), available at [www.xfem.rwth-aachen.de/Background/Download/XFEM\\_Download.php](http://www.xfem.rwth-aachen.de/Background/Download/XFEM_Download.php). The authors gratefully acknowledge this resource. The authors also thank Professor Dominik Schoetzau (University of British Columbia) for fruitful discussions. This work was partially funded by the NSERC Discovery Grants program, which both authors gratefully acknowledge.

## Appendix A: Variational formulation of the $P\&W$ scheme

In this appendix we present the derivation of the variational formulation of the  $P\&W$  scheme, using the definitions given in Sections 2.2 and 3.2.

In view of the domain decomposition  $V = V_o \cup V_*$ , the elastic problem associated with the  $P\&W$  scheme is formulated in the strong form as follows:

$$\nabla \cdot \boldsymbol{\sigma} + \mathbf{f} = \mathbf{0}, \quad \boldsymbol{\varepsilon}(\mathbf{u}) - \mathcal{C}^{-1} : \boldsymbol{\sigma} = \mathbf{0} \quad \text{in } V_* \quad (41)$$

$$\nabla \cdot \boldsymbol{\sigma}(\mathbf{u}) + \mathbf{f} = \mathbf{0} \quad \text{in } V_o \quad (42)$$

$$\boldsymbol{\sigma}^\pm(\mathbf{u}) \cdot \mathbf{n} = -p_c \mathbf{n} + \hat{\sigma}_s \mathbf{s} \quad \text{on } \Sigma_c \cap V_o \quad (43)$$

$$\boldsymbol{\sigma}^\pm \cdot \mathbf{n} = -p_c \mathbf{n} + \hat{\sigma}_s \mathbf{s} \quad \text{on } \Sigma_c \cap V_* \quad (44)$$

$$\mathbf{s} \cdot \boldsymbol{\sigma}^\pm \cdot \mathbf{n} = \hat{\sigma}_s \quad \text{on } \Sigma_t \quad (45)$$

$$[[\mathbf{u}]] \cdot \mathbf{n} = w_t, \quad \mathbf{n} \cdot [[\boldsymbol{\sigma}]] \cdot \mathbf{n} = 0 \quad \text{on } \Sigma_t \quad (46)$$

$$[[\mathbf{u}]]_{\partial V_*} = 0, \quad [[\boldsymbol{\sigma}]]_{\partial V_*} \cdot \mathbf{n}_* = 0 \quad \text{on } \partial V_* \quad (47)$$

$$\mathbf{u} = \mathbf{g} \quad \text{on } \Gamma \quad (48)$$

Above, the unit normal vector along  $\partial V_*$  is denoted  $\mathbf{n}_*$  and is consistent with the outward normal direction for the domain  $V_*$ . We also define the displacement jump along  $\partial V_*$  via  $[[\mathbf{u}]]_{\partial V_*} = \mathbf{u}_o - \mathbf{u}_*$  where  $\mathbf{u}_o$  and  $\mathbf{u}_*$  denote the values of  $\mathbf{u}$  in the domains  $V_o$  and  $V_*$ , respectively; the stress jump is defined similarly. To complete the problem, the boundary conditions (46) and (47), that enforce a displacement jump or the displacement continuity, are supplemented with the continuity of traction in the direction of the enforced jumps.

The weak form (15) - (18) can be obtained by setting to zero the first variation of the following mixed hybrid potential,

$$\Pi(\mathbf{u}, \boldsymbol{\sigma}, \mathbf{t}_\Sigma, \mathbf{t}_*) = \int_{V_o \setminus \Sigma} \left[ \frac{1}{2} \boldsymbol{\sigma}(\mathbf{u}) : \boldsymbol{\varepsilon}(\mathbf{u}) - \mathbf{f} \cdot \mathbf{u} \right] dV \quad (49)$$

$$+ \int_{\Sigma_c \cap V_o} (-p_c \mathbf{n} + \hat{\sigma}_s \mathbf{s}) \cdot [[\mathbf{u}]] ds \quad (50)$$

$$+ \int_{V_* \setminus \Sigma} \left[ \boldsymbol{\sigma} : \boldsymbol{\varepsilon}(\mathbf{u}) - \frac{1}{2} \boldsymbol{\sigma} : \mathcal{C}^{-1} \boldsymbol{\sigma} - \mathbf{f} \cdot \mathbf{u} \right] dV \quad (51)$$

$$+ \int_{\Sigma_c \cap V_*} (-p_c \mathbf{n} + \hat{\sigma}_s \mathbf{s}) \cdot [[\mathbf{u}]] ds \quad (52)$$

$$+ \int_{\Sigma_t} [\hat{\sigma}_s ([[ \mathbf{u} ]]) \cdot \mathbf{s} + (\mathbf{n} \cdot \mathbf{t}_\Sigma) ([[ \mathbf{u} ]]) \cdot \mathbf{n} - w_t] ds \quad (53)$$

$$+ \int_{\partial V_*} \mathbf{t}_* \cdot [[\mathbf{u}]]_{\partial V_*} ds \quad (54)$$

This functional is a combination of the potential energy functional for the domain  $V_o$  ((49), (50)), the hybrid Hellinger-Reissner potential [43, 44, 45, 46] for the domain  $V_*$  ((51) - (53)), and the interface potential (54) that is used to introduce the continuity of displacement across the interface  $\partial V_*$  between  $V_o$  and  $V_*$  [46]. To impose the displacement jump constraints within the hybrid variational principle [46], we introduce two independent interface variables, namely: the traction vector  $\mathbf{t}_\Sigma$  along  $\Sigma_t$  that is consistent with the normal direction on the side  $\Sigma^-$ , and the traction vector  $\mathbf{t}_*$  along  $\partial V_*$  that is consistent with the outward normal direction for the domain  $V_*$ . We

consider the variation  $\delta \mathbf{u}$  of the displacement in  $V$ , the variation  $\delta \boldsymbol{\sigma}$  of the stress in  $V_*$ , and the variations  $\delta \mathbf{t}_\Sigma$  and  $\delta \mathbf{t}_*$  of the traction vectors  $\mathbf{t}_\Sigma$  and  $\mathbf{t}_*$ , respectively. The first variation of the potential (49) - (54) has the following form:

$$0 = \delta \Pi = \int_{V_o \setminus \Sigma} [\boldsymbol{\sigma}(\mathbf{u}) : \boldsymbol{\varepsilon}(\delta \mathbf{u}) - \mathbf{f} \cdot \delta \mathbf{u}] dV \quad (55)$$

$$+ \int_{\Sigma_c} (-p_c \mathbf{n} + \hat{\sigma}_s \mathbf{s}) \cdot [[\delta \mathbf{u}]] ds + \int_{\Sigma_t} \hat{\sigma}_s ([[ \delta \mathbf{u} ]] \cdot \mathbf{s}) ds \quad (56)$$

$$+ \int_{V_* \setminus \Sigma} [(\boldsymbol{\varepsilon}(\mathbf{u}) - \mathcal{C}^{-1} \boldsymbol{\sigma}) : \delta \boldsymbol{\sigma} + \boldsymbol{\sigma} : \boldsymbol{\varepsilon}(\delta \mathbf{u}) - \mathbf{f} \cdot \delta \mathbf{u}] dV \quad (57)$$

$$+ \int_{\Sigma_t} [(\mathbf{n} \cdot \delta \mathbf{t}_\Sigma) ([[ \mathbf{u} ]] \cdot \mathbf{n} - w_t) + (\mathbf{n} \cdot \mathbf{t}_\Sigma) ([[ \delta \mathbf{u} ]] \cdot \mathbf{n})] ds \quad (58)$$

$$+ \int_{\partial V_*} [\delta \mathbf{t}_* \cdot [[ \mathbf{u} ]]_{\partial V_*} + \mathbf{t}_* \cdot [[ \delta \mathbf{u} ]]_{\partial V_*}] ds \quad (59)$$

After integration by parts is performed, the following variational form is obtained:

$$0 = - \int_{V_o \setminus \Sigma} (\nabla \cdot \boldsymbol{\sigma}(\mathbf{u}) + \mathbf{f}) \delta \mathbf{u} dV \quad (60)$$

$$+ \int_{V_* \setminus \Sigma} [-(\nabla \cdot \boldsymbol{\sigma} + \mathbf{f}) \delta \mathbf{u} + (\boldsymbol{\varepsilon}(\mathbf{u}) - \mathcal{C}^{-1} \boldsymbol{\sigma}) : \delta \boldsymbol{\sigma}] dV \quad (61)$$

$$+ \int_{\Sigma_c \cap V_o} [(-\{\boldsymbol{\sigma}(\mathbf{u})\} \cdot \mathbf{n} - p_c \mathbf{n} + \hat{\sigma}_s \mathbf{s}) \cdot [[ \delta \mathbf{u} ]] - ([[ \boldsymbol{\sigma}(\mathbf{u}) ]] \cdot \mathbf{n}) \cdot \{\delta \mathbf{u}\}] ds \quad (62)$$

$$+ \int_{\Sigma_c \cap V_*} [(-\{\boldsymbol{\sigma}\} \cdot \mathbf{n} - p_c \mathbf{n} + \hat{\sigma}_s \mathbf{s}) \cdot [[ \delta \mathbf{u} ]] - ([[ \boldsymbol{\sigma} ]] \cdot \mathbf{n}) \cdot \{\delta \mathbf{u}\}] ds \quad (63)$$

$$+ \int_{\Sigma_t} [(-\mathbf{s} \cdot \{\boldsymbol{\sigma}\} \cdot \mathbf{n} + \hat{\sigma}_s) ([[ \delta \mathbf{u} ]] \cdot \mathbf{s}) - ([[ \boldsymbol{\sigma} ]] \cdot \mathbf{n}) \cdot \{\delta \mathbf{u}\}] ds \quad (64)$$

$$+ \int_{\Sigma_t} [(\mathbf{n} \cdot \delta \mathbf{t}_\Sigma) ([[ \mathbf{u} ]] \cdot \mathbf{n} - w_t) + (\mathbf{n} \cdot \mathbf{t}_\Sigma - \mathbf{n} \cdot \{\boldsymbol{\sigma}\} \cdot \mathbf{n}) ([[ \delta \mathbf{u} ]] \cdot \mathbf{n})] ds \quad (65)$$

$$+ \int_{\partial V_*} [\delta \mathbf{t}_* \cdot [[\mathbf{u}]]_{\partial V_*} + (\mathbf{t}_* - \{\boldsymbol{\sigma}\}_{\partial V_*} \cdot \mathbf{n}_*) \cdot [[\delta \mathbf{u}]]_{\partial V_*} - ([[ \boldsymbol{\sigma} ]]_{\partial V_*} \cdot \mathbf{n}_*) \cdot \{\delta \mathbf{u}\}_{\partial V_*}] ds \quad (66)$$

Above, the average values along  $\partial V_*$  are defined by  $\{\delta \mathbf{u}\}_{\partial V_*} = (\delta \mathbf{u}_o + \delta \mathbf{u}_*)/2$  where  $\delta \mathbf{u}_o$  and  $\delta \mathbf{u}_*$  denote the limiting values of  $\delta \mathbf{u}$  in the domains  $V_o$  and  $V_*$ , respectively; and  $\{\boldsymbol{\sigma}\}_{\partial V_*} = (\boldsymbol{\sigma}(\mathbf{u}_o) + \boldsymbol{\sigma})/2$ .

On the account of the fact that independent variations can be arbitrary, we recover the strong form of Eqs. (41) - (45) using (60) - (64). Further, (65), together with the last term in (64), and (66) recover the strong form of Eqs. (46) and (47) and additionally impose the conditions:

$$\mathbf{n} \cdot \mathbf{t}_\Sigma = \mathbf{n} \cdot \{\boldsymbol{\sigma}\} \cdot \mathbf{n} \quad (67)$$

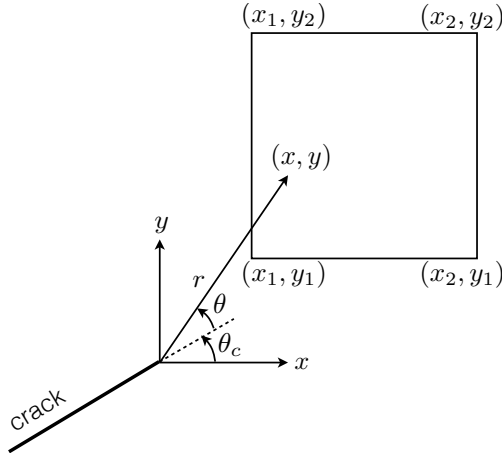
$$\mathbf{t}_* = \{\boldsymbol{\sigma}\}_{\partial V_*} \cdot \mathbf{n}_* \quad (68)$$

Thus, the governing equations are recovered in the strong form, except for the Dirichlet boundary condition (48), which is satisfied by the choice of the solution from the space  $\mathcal{U}_\mathbf{u}^h$  of functions that satisfy (48).

The discretized weak form (15) - (18) is obtained from Eqs. (55) - (59), by using  $\mathbf{v} = \delta \mathbf{u}$  and  $\boldsymbol{\tau} = \delta \boldsymbol{\sigma}$ , and on account of the fact that we choose the test and trial functions,  $\mathbf{u}$  and  $\mathbf{v}$ , to be continuous across  $\partial V_*$ , thus the terms (59) are not involved, as in the derivation in [40]. Finally, we choose the traction vector  $\mathbf{t}_\Sigma$  to satisfy (67) exactly, in order to obtain the weak form similar to that used in [40]. In other words, we use the average normal traction  $\mathbf{n} \cdot \{\boldsymbol{\sigma}\} \cdot \mathbf{n}$  as a work conjugate for the normal displacement jump across the crack.

Alternatively, the weak form (15) - (18) can be obtained following the derivation in [40]. Each equation in (41) - (47) is multiplied by an arbitrary function of a suitable dimension, that is generally a work conjugate of the displacement, stress, displacement jump, etc., and the result is integrated over the corresponding domain or boundary, after which integration by parts is used. The derivation in [40] omits the traction continuity conditions along the boundaries for which the displacement continuity or the displacement jump is prescribed. However it is seen from the above components (64) - (66) of the variational formulation that it is necessary to include the traction continuity conditions in the boundary conditions (46) and (47) to complement enforced displacement jumps and enforced displacement continuity.

Figure 12: Quadrilateral element aligned with Cartesian axes, and crack-tip polar coordinates.



The present variational formulation additionally justifies the use of the normal traction  $\mathbf{n} \cdot \{\boldsymbol{\sigma}\} \cdot \mathbf{n}$  as a work conjugate for the normal displacement jump across the crack in (18).

### Appendix B: Linear dependence of power law crack-tip enrichment in a bi-linear element

Consider a bi-linear element aligned with the Cartesian axes, with the nodes placed at  $(x_1, y_1)$ ,  $(x_2, y_1)$ ,  $(x_2, y_2)$  and  $(x_1, y_2)$ , as shown in Fig 12. The side-lengths of the element are denoted by  $h_x = x_2 - x_1$  and  $h_y = y_2 - y_1$ . Consider a crack-tip segment inclined to the  $x$ -axis by an angle  $\theta_c$ . We assume that all nodes of the element are enriched with the power law displacement tip enrichment (30), where  $(r, \theta)$  are the polar coordinates centered at the fracture tip, so that the values  $\theta = \pm\pi$  correspond to the two crack faces. Without loss of generality, the crack tip is placed at the origin of the coordinate system  $(0, 0)$ . The Cartesian coordinates of a point  $\mathbf{x}$  are given by  $x = r \cos \hat{\theta}$ ,  $y = r \sin \hat{\theta}$ , where  $\hat{\theta} = \theta + \theta_c$ .

The bi-linear Lagrange shape functions  $N_i(\mathbf{x})$  associated with the element nodes  $i = 1, \dots, 4$  can be expressed in polar coordinates as

$$N_1(\mathbf{x}) = \frac{1}{h_x h_y} (r \cos \hat{\theta} - x_2)(r \sin \hat{\theta} - y_2),$$

$$\begin{aligned}
N_2(\mathbf{x}) &= \frac{-1}{h_x h_y} (r \cos \hat{\theta} - x_1)(r \sin \hat{\theta} - y_2), \\
N_3(\mathbf{x}) &= \frac{1}{h_x h_y} (r \cos \hat{\theta} - x_1)(r \sin \hat{\theta} - y_1), \\
N_4(\mathbf{x}) &= \frac{-1}{h_x h_y} (r \cos \hat{\theta} - x_2)(r \sin \hat{\theta} - y_1)
\end{aligned} \tag{69}$$

We seek to express functions  $N_i(\mathbf{x})\psi_j^{\mathbf{u},\lambda}(\mathbf{x})$  for  $i = 4$  and  $j = 3, 4$  as a linear combination of the remaining fourteen of the total sixteen singular shape functions  $N_i(\mathbf{x})\psi_j^{\mathbf{u},\lambda}(\mathbf{x})$  ( $i, j = 1, \dots, 4$ ). This can be achieved by finding two  $4 \times 4$  matrices  $\mathbf{A}$  with entries  $A_{ij}$  such that

$$\sum_{i,j=1}^4 A_{ij} N_i(\mathbf{x})\psi_j^{\mathbf{u},\lambda}(\mathbf{x}) = 0 \quad \text{for all } \mathbf{x} \tag{70}$$

and such that either

$$A_{43} = 1, \quad A_{44} = 0 \tag{71}$$

or

$$A_{43} = 0, \quad A_{44} = 1 \tag{72}$$

In matrix form, Eq. (70) reads

$$\mathbf{N}^T(r, \theta) \mathbf{A} \Phi(\theta) = 0 \quad \text{for all } (r, \theta) \tag{73}$$

in which

$$\begin{aligned}
\mathbf{N}(r, \theta) &= h_x h_y \times [N_1(\mathbf{x}), N_2(\mathbf{x}), N_3(\mathbf{x}), N_4(\mathbf{x})]^T \\
\Phi(\theta) &= [\sin(\lambda\theta), \cos(\lambda\theta), \sin(\lambda - 2)\theta, \cos(\lambda - 2)\theta]^T
\end{aligned}$$

The bi-linear shape functions (69) can be expanded into powers of  $r$  via

$$\mathbf{N}(r, \theta) = r^2 \sin \hat{\theta} \cos \hat{\theta} \mathbf{v}_2 + r(\cos \theta \mathbf{v}_1^1 + \sin \theta \mathbf{v}_1^2) + \mathbf{v}_0 \tag{74}$$

in which the vectors  $\mathbf{v}_2$ ,  $\mathbf{v}_1^1$ ,  $\mathbf{v}_1^2$  and  $\mathbf{v}_0$  do not depend on  $r$  and  $\theta$ . Combining Eqs. (73) and (74) makes it possible to separate equations associated with different powers of  $r$ . In particular, we get

$$\mathbf{v}_2^T \mathbf{A} \Phi(\theta) = 0, \quad \mathbf{v}_0^T \mathbf{A} \Phi(\theta) = 0, \quad \text{for all } \theta \tag{75}$$

Because the functions in  $\Phi(\theta)$  are linearly-independent, (75) implies the following eight equations for the unknown entries  $A_{ij}$ :

$$\mathbf{v}_2^T \mathbf{A} = \mathbf{0}, \quad \mathbf{v}_0^T \mathbf{A} = \mathbf{0} \quad (76)$$

Separating the terms linear in  $r$  in Eq. (73) implies that

$$(\cos \theta \mathbf{c}_1 + \sin \theta \mathbf{c}_2)^T \Phi(\theta) = 0 \quad \text{for all } \theta \quad (77)$$

where  $\mathbf{c}_k = \mathbf{A}^T \mathbf{v}_1^k$  for  $k = 1, 2$ . The entries of the vector  $\mathbf{c}_k$  are linear combinations of the unknown entries  $A_{ij}$  and are denoted by  $c_{km}$  for  $m = 1, \dots, 4$ . By substituting  $\theta = 0, \pi, \pm\pi/2$  into (77), we obtain the following four equations for  $A_{ij}$ :

$$c_{12} + c_{14} = 0, \quad c_{11} + c_{13} = 0, \quad c_{22} - c_{24} = 0, \quad c_{21} - c_{23} = 0 \quad (78)$$

Using (77) and (78), one can also obtain the following two equations:

$$c_{11} + c_{22} = 0, \quad c_{12} - c_{21} = 0 \quad (79)$$

Finally, combining eight equations (76), four equations (78), two equations (79) and two equations from either (71) or (72), we obtain sixteen equations for the sixteen unknown entries  $A_{ij}$ . In all numerical tests performed, these sixteen equations were found to be linearly independent and this procedure resulted in successful elimination of the linearly-dependent shape functions from the XFEM formulation.

This confirms that we can express two functions  $N_i(\mathbf{x})\psi_j^{\mathbf{u},\lambda}(\mathbf{x})$  for  $i = 4$  and  $j = 3, 4$  through the rest fourteen of the total sixteen functions  $N_i(\mathbf{x})\psi_j^{\mathbf{u},\lambda}(\mathbf{x})$ , without the need to explicitly construct matrix  $\mathbf{A}$ .

It can be seen that the stress enrichment (31) can be expressed via the displacement enrichment (30) as

$$\boldsymbol{\psi}^{\boldsymbol{\sigma},\lambda}(r, \theta) = \boldsymbol{\psi}^{\mathbf{u},\lambda-1}(r, \theta) \quad (80)$$

Therefore, the above derivation applies to the stress shape functions, upon the change of  $\lambda$  to  $\lambda - 1$ .

- [1] E. Gordeliy, A. P. Peirce, Coupling schemes for modeling hydraulic fracture propagation using the XFEM, *Comput. Methods Appl. Mech. Engrg.* 253 (2013) 305–322.

- [2] E. Gordeliy, A. P. Peirce, Implicit level set schemes for modeling hydraulic fractures using the XFEM, *Comput. Methods Appl. Mech. Engrg.* 266 (2013) 125–143.
- [3] D. Spence, D. Turcotte, Magma-driven propagation crack, *J. Geophys. Res.* 90 (1985) 575–580.
- [4] J. Lister, R. Kerr, Fluid-mechanical models of crack propagation and their application to magma transport in dykes, *J. Geophys. Res.* (1991) 10,049–10,077.
- [5] A. Rubin, Propagation of magma-filled cracks, *Ann. Rev. Earth & Planetary Sci.* 23 (1995) 287–336.
- [6] J. R. Lister, Buoyancy-driven fluid fracture: similarity solutions for the horizontal and vertical propagation of fluid-filled cracks, *J. Fluid Mech.* 217 (1990) 213–239.
- [7] S. M. Roper, J. R. Lister, Buoyancy-driven crack propagation from an over-pressured source, *J. Fluid Mech.* 536 (2005) 79–98.
- [8] S. Roper, J. Lister, Buoyancy-driven crack propagation: the limit of large fracture toughness, *J. Fluid Mech.* 580 (2007) 359–380. doi:doi:10.1017/S0022112007005472.
- [9] J. R. Rice, V. C. Tsai, Outburst flooding under ice sheets as turbulently driven hydraulic fracture, in: *Proc. 16th U.S. National Congress of Theoretical and Applied Mechanics*, no. Extended Abstract 368, ASME, New York, 2010.
- [10] V. C. Tsai, J. R. Rice, A model for turbulent hydraulic fracture and application to crack propagation at glacier beds, *J. Geophys. Res.* 115 (2010) F03007. doi:Hydraulic Fracturing/TsRi10.pdf.
- [11] U. Frank, N. Barkley, Remediation of low permeability subsurface formations by fracturing enhancements of soil vapor extraction, *Journal of Hazardous Materials* 40 (191–201).
- [12] L. Murdoch, Mechanical analysis of idealized shallow hydraulic fracture, *J. Geotech. Geoenviron.* 128 (6) (2002) 488–495.

- [13] L. C. Murdoch, W. W. Slack, Forms of hydraulic fractures in shallow fine-grained formations, *J. Geotech. Geoenviron.* 128 (6) (2002) 479–487.
- [14] A. Abou-Sayed, D. Andrews, I. Buhidma, Evaluation of oily waste injection below the permafrost in Prudhoe Bay field, in: *Proceedings of the California Regional Meetings*, Bakersfield, CA, Society of Petroleum Engineers, Richardson, TX, 1989, pp. 129–142.
- [15] R. Jeffrey, K. Mills, Hydraulic fracturing applied to inducing longwall coal mine goaf falls, in: *Pacific Rocks 2000*, Balkema, Rotterdam, 2000, pp. 423–430.
- [16] A. van As, R. Jeffrey, Caving induced by hydraulic fracturing at Northparkes mines, in: *Pacific Rocks 2000*, Balkema, Rotterdam, 2000, pp. 353–360.
- [17] J. Gidley, S. Holditch, D. Nierode, R. Veatch (Eds.), *Recent Advances in Hydraulic Fracturing*, Vol. 12 of SPE Monograph Series, Society of Petroleum Engineers, Richardson TX, 1989.
- [18] P. Valkó, M. Economides, *Hydraulic Fracture Mechanics*, John Wiley & Sons, Chichester UK, 1995.
- [19] M. Economides, K. Nolte (Eds.), *Reservoir Stimulation*, 3rd Edition, John Wiley & Sons, Chichester UK, 2000.
- [20] R. Clifton, Three-dimensional fracture-propagation models, in: J. Gidley, S. Holditch, D. Nierode, R. Veatch (Eds.), *Recent Advances in Hydraulic Fracturing – SPE Monographs Vol. 12*, Society of Petroleum Engineers, 1989, pp. 95–108.
- [21] A. Peirce, E. Siebrits, The scaled flexibility matrix method for the efficient solution of boundary value problems in 2D and 3D layered elastic media, *Computer Meth. Appl. Mech. Eng.* 190 (2001) 5935–5956.
- [22] A. Peirce, E. Siebrits, Uniform asymptotic approximations for accurate modeling of cracks in layered elastic media, *Int. J. Fracture* 110 (2001) 205–239.
- [23] E. Siebrits, A. Peirce, An efficient multi-layer planar 3D fracture growth algorithm using a fixed mesh approach, *Int. J. Numer. Meth. Engng.* 53 (2002) 691–717.

- [24] A. Peirce, E. . Siebrits, A dual mesh multigrid preconditioner for the efficient solution of hydraulically driven fracture problems, *Int. J. Numer. Meth. Engng.* 63 (2005) 1797–1823.
- [25] A. P. Peirce, Localized Jacobian ILU preconditioners for hydraulic fractures, *Int. J. Numer. Meth. Engng.* 65 (12) (2006) 1935–1946.
- [26] J. Adachi, E. . Siebrits, A. P. Peirce, J. Desroches, Computer simulation of hydraulic fractures, *Int. J. Rock Mech. Min. Sci.* 44 (5) (2007) 739–757.  
URL <http://www.sciencedirect.com/science/article/B6V4W-4N08V5H-1/2/458efc93ac>
- [27] A. P. Peirce, E. Detournay, An implicit level set method for modeling hydraulically driven fractures, *Computer Meth. Appl. Mech. Eng.* 197 (2008) 2858–2885. doi:doi:10.1016/j.cma.2008.01.013.
- [28] A. R. Ingraffea, T. J. Boone, D. V. Swenson, *Computer Simulation of Fracture Processes*, 1991, Ch. 12.
- [29] K. Shah, B. Carter, A. Ingraffea, Hydraulic fracturing simulation in parallel computing environments, *Int. J. Rock Mech. Min. Sci.* 34 (3/4) (1997) 474.
- [30] N. Moës, J. Dolbow, T. Belytschko, A finite element method for crack growth without remeshing, *Int. J. Numer. Meth. Engng* 46 (1999) 131–150.
- [31] M. Stolarska, D. Chopp, N. Moes, T. Belytschko, Modeling crack growth by level sets and the extended finite element method, *Int. J. Numer. Meth. Engng.* 51 (2001) 943–960.
- [32] N. Sukumar, J.-H. Prevost, Modeling quasi-static crack growth with the extended finite element method Part I: Computer implementation., *Int. J. Solids Structures* 40 (2003) 7513–7537.
- [33] A. Taleghani, Analysis of hydraulic fracture propagation in fractured reservoirs: an improved model for the interaction between induced and natural fractures, Phd thesis, The University of Texas at Austin, The University of Texas at Austin (May 2009).

- [34] Q.-W. Ren, Y.-W. Dong, T. T. Yu, Numerical modeling of concrete hydraulic fracturing with extended finite element method, *Science in China Series E: Technological Sciences* 52 (2009) 559–565.
- [35] E. Detournay, Propagation regimes of fluid-driven fractures in impermeable rocks, *Int. J. Geomechanics* 4 (1) (2004) 1–11.
- [36] B. Lecampion, An extended finite element method for hydraulic fracture problems, *Commun. Numer. Meth. Engng.* 25 (2009) 121–133.
- [37] J. Desroches, E. Detournay, B. Lenoach, P. Papanastasiou, J. Pearson, M. Thiercelin, A.-D. Cheng, The crack tip region in hydraulic fracturing, *Proc. Roy. Soc. London, Ser. A* 447 (1994) 39–48.
- [38] T.-P. Fries, A corrected XFEM approximation without problems in blending element, *Int. J. Numer. Meth. Engng* 75 (2008) 503–532.
- [39] E. Detournay, A. P. Peirce, On the moving boundary conditions for a hydraulic fracture, *Int. J. Engng. Sci.*In press.
- [40] A. Zilian, T.-P. Fries, A localized mixed-hybrid method for imposing interfacial constraints in the extended finite element method (XFEM), *Int. J. Numer. Meth. Engng* 79 (2009) 733–752.
- [41] O. C. Zienkiewicz, R. L. Taylor, D. D. Fox, *The Finite Element Method for Solid and Structural Mechanics*, 7th Edition, Elsevier, 2014.
- [42] J. R. Barber, *Elasticity*, Kluwer Academic Publishers, Dordrecht, 1992.
- [43] E. Hellinger, Die allgemeinen ansatze der mechanik der kontinua, *Enz. Math. Wis* 4 (1914) 602–694.
- [44] E. Reissner, On a variational theorem in elasticity, *J Math Phys* 29 (1950) 90 – 95.
- [45] E. Reissner, A note on variational theorems in elasticity, *Int. J. Solids Structures* 1 (1965) 93 – 95.
- [46] J. T. Oden, J. N. Reddy, *Variational Methods in Theoretical Mechanics*, Springer-Verlag Berlin Heidelberg, 1976.

- [47] A. P. Peirce, A Hermite cubic collocation scheme for plane strain hydraulic fractures, *Computer Meth. Appl. Mech. Eng.* 199 (29-32) (2010) 1949–1962. doi:10.1016/j.cma.2010.02.009.
- [48] T.-P. Fries, T. Belytschko, The extended/generalized finite element method: An overview of the method and its applications, *Int. J. Numer. Meth. Engng.* 84 (2010) 253–304.
- [49] I. Babuska, J. M. Melenk, The partition of unity method, *Int. J. Numer. Meth. Engng* 40 (1997) 727–758.
- [50] P. Laborde, J. Pommier, Y. Renard, M. Salaün, High-order extended finite element method for cracked domains, *Int. J. Numer. Meth. Engng* 64 (2005) 354–381.
- [51] G. Ventura, R. Gracie, T. Belytschko, Fast integration and weight function blending in the extended finite element method, *Int. J. Numer. Meth. Engng* 77 (2009) 1–29.
- [52] G. N. Wells, L. J. Sluys, A new method for modelling cohesive cracks using finite elements, *Int. J. Numer. Meth. Engng* 50 (2001) 2667—2682.
- [53] J. Dolbow, N. Moës, T. Belytschko, Discontinuous enrichment in finite elements with a partition of unity method, *Finite Elements in Analysis and Design* 36 (2000) 235–260.
- [54] G. Zi, T. Belytschko, New crack-tip elements for xfem and applications to cohesive cracks, *Int. J. Numer. Meth. Engng* 57 (2003) 2221—2240.
- [55] S. Mariani, U. Perego, Extended finite element method for quasi-brittle fracture, *Int. J. Numer. Meth. Engng.* 58 (2003) 103–126.
- [56] N. Moës, J. Dolbow, T. Belytschko, A finite element method for crack growth without remeshing, *Int. J. Numer. Meth. Engng.* 46 (1999) 131–150.
- [57] T. Belytschko, T. Black, Elastic crack growth in finite elements with minimal remeshing, *Int. J. Numer. Meth. Engng.* 45 (1999) 601–620.
- [58] M. L. Williams, Stress singularities resulting from various boundary conditions in angular corners of plates in extension, *ASME Journal of Applied Mechanics* 19 (1952) 526–528.

- [59] M. L. Williams, The bending stress distribution at the base of a stationary crack, *ASME Journal of Applied Mechanics* 28 (1961) 78–82.
- [60] R. Huang, J. H. Prevost, Z. Y. Huang, Z. Suo, Channel-cracking of thin films with the extended finite element method, *Engineering Fracture Mechanics* 70 (2003) 2513–2526.
- [61] A. R. Zak, M. L. Williams, Crack point stress singularities at a bi-material interface, *Journal of Applied Mechanics* 30 (1963) 142–143.
- [62] S. Loehnert, D. S. Mueller-Hoeppe, P. Wriggers, 3d corrected XFEM approach and extension to finite deformation theory, *Int. J. Numer. Meth. Engng* 86 (2011) 431–452.